






Prestressed elasticity of amorphous solids

Shang Zhang ¹, Ethan Stanifer ¹, Vishwas V. Vasisht², Leyou Zhang ^{1,*}, Emanuela Del Gado ³, and Xiaoming Mao ^{1,†}

¹*Department of Physics, University of Michigan, Ann Arbor, Michigan 48109-1040, USA*

²*Department of Physics, Indian Institute of Technology, Palakkad 678623, India*

³*Department of Physics, Institute for Soft Matter Synthesis and Metrology, Georgetown University, Washington D.C. 20057, USA*



(Received 25 June 2022; accepted 24 September 2022; published 12 December 2022)

Prestress in amorphous solids bears the memory of their formation and plays a profound role in their mechanical properties. Here we develop a set of mathematical tools to investigate mechanical response of prestressed systems, using stress rather than strain as the fundamental variable. This theory allows microscopic prestress to vary for the same bond or contact configuration and is particularly convenient for nonconservative systems, such as granular packings and jammed suspensions, where there is no well-defined reference state, invalidating conventional elasticity. Using prestressed nonconservative triangular lattices and a computational model of amorphous solids, we show that drastically different mechanical responses can show up in amorphous materials at the same density, due to nonconservative interactions which evolve over time, or different preparation protocols. In both cases, the information is encoded in the prestress of the network and not visible at all from the configurations of the network in the case of nonconservative interactions.

DOI: [10.1103/PhysRevResearch.4.043181](https://doi.org/10.1103/PhysRevResearch.4.043181)

I. INTRODUCTION

Almost all solid materials are stressed. Amorphous solids exhibit quenched residual stress from their preparation process, crystalline solids are stressed by defects and grain-boundaries, and living matter experiences active stress from biological processes. The ubiquity of stressed solids is encapsulated in the fact that the stress tensor σ , as a $d \times d$ symmetrical matrix in d dimensions, has $d(d+1)/2$ independent degrees of freedom, but the force balance equation,

$$\partial_j \sigma_{ij} = 0, \quad (1)$$

only poses d constraints, leaving $d(d-1)/2$ unconstrained components in the stress field. In absence of external load, all components have to vanish if the material, and the stress field, have to be homogeneous, but they can be nonzero at length-scales over which heterogeneities or excess constraints are present (“geometric frustration”), giving rise to *prestress* (also known as “residual stress”, “initial stress” or “eigenstress” in different contexts) [1,2].

In structural engineering, prestress is proactively used to modify both stability and load bearing capability of structures, from prestressed reinforced concrete to tensegrity architectures [Figs. 1(a), 1(h) and 1(j)]. In materials, instead, prestresses can emerge spontaneously, as the direct

consequence of out-of-equilibrium processes through which they solidify, or of the external load applied during processing. Prominent examples include isotropic compressive prestress in jammed packings [3] or tensile prestress in gels [4], shear prestress in shear jammed granular matter [5] and shear thickened dense suspensions [6], isotropic prestresses in glasses [7], and rich varieties of anisotropic prestress fields in prestressed/tensegrity metamaterials [8–13], and biological systems [14–16] [Figs. 1(b)–1(g) and 1(i)]. Remarkably, very much in the same way as for buildings and large scale structures, microscopic residual stresses in amorphous solids may strongly affect their strength—stiffen or soften them, and direct their dynamical response [1,3,17–39].

A deep understanding of the consequences of prestress is therefore key to predict elasticity and material properties in general, but prestresses can be very elusive, since it is difficult to directly access them in experiments and in most cases only their indirect consequences can be detected. Current studies of amorphous solids, such as glasses and jamming of frictionless particles, typically treat prestress as a field solely determined by the distance from the ideal jamming transition as interactions between particles are modeled as conservative springs (e.g., $p \sim \delta z$ where p is compressional prestress and δz is the excess coordination close to the jamming threshold), and thus all scaling relations obtained are controlled by this variable [3,43–50].

However, in a broad range of amorphous materials, the characteristics of prestress exhibit far more complexity. First, prestress can strongly depend on the *preparation history* of the material, and this is especially prominent in denser samples, relatively far from the jamming threshold [19,20,51]. The nonequilibrium process during which the system solidify encodes complex local spatial organization or order, and interestingly, the effects of this local order on mechanical

*Present address: Google Cloud AI, Pittsburgh, PA, 15206, USA

†maox@umich.edu

Published by the American Physical Society under the terms of the [Creative Commons Attribution 4.0 International license](https://creativecommons.org/licenses/by/4.0/). Further distribution of this work must maintain attribution to the author(s) and the published article’s title, journal citation, and DOI.

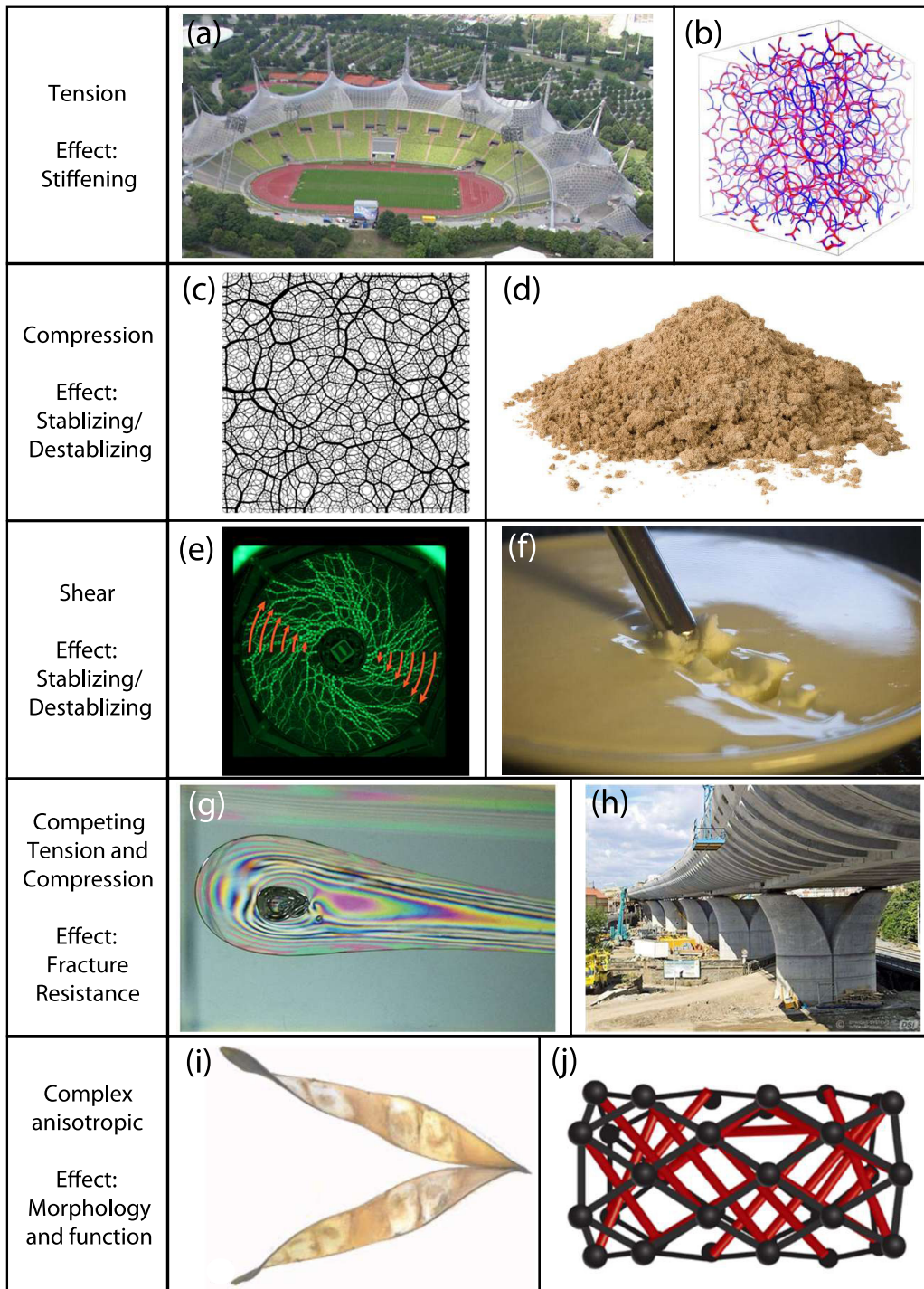


FIG. 1. A series of examples of stressed materials including structures under tension [a tensile net architecture in (a) and a model colloidal gel [4] in (b)], structures under compression [contact network of a jammed packing of repulsive disks [40] (c) and pile of sand (d)], structures under shear [shear jamming of photoelastic discs (e) and an acoustically tunable shear thickening fluid (image taken by Neil Lin) (f)], structures under competing tensile and compressive forces [a Prince Rupert's drop [41] in (g) and a bridge made from prestressed concrete in (h)], as well as systems with more complex modes of stress [a pea pod which uses stress to open [14] in (i) and a tensegrity metamaterial [42] in (j)].

response are reflected through prestress. Second, colloidal and macroscale amorphous solids (e.g., jammed suspensions and granular packings) are often characterized by *nonconservative*, frictional and history-dependent interactions between particles, in contrast to simple conservative and two-body

interactions typically used to describe atomistic and molecular degrees of freedom in supercooled liquids and related glasses. The more complex and history-dependent interactions make the microscopic prestress *underdetermined* from a macroscopic configuration, allowing dramatic change in stress

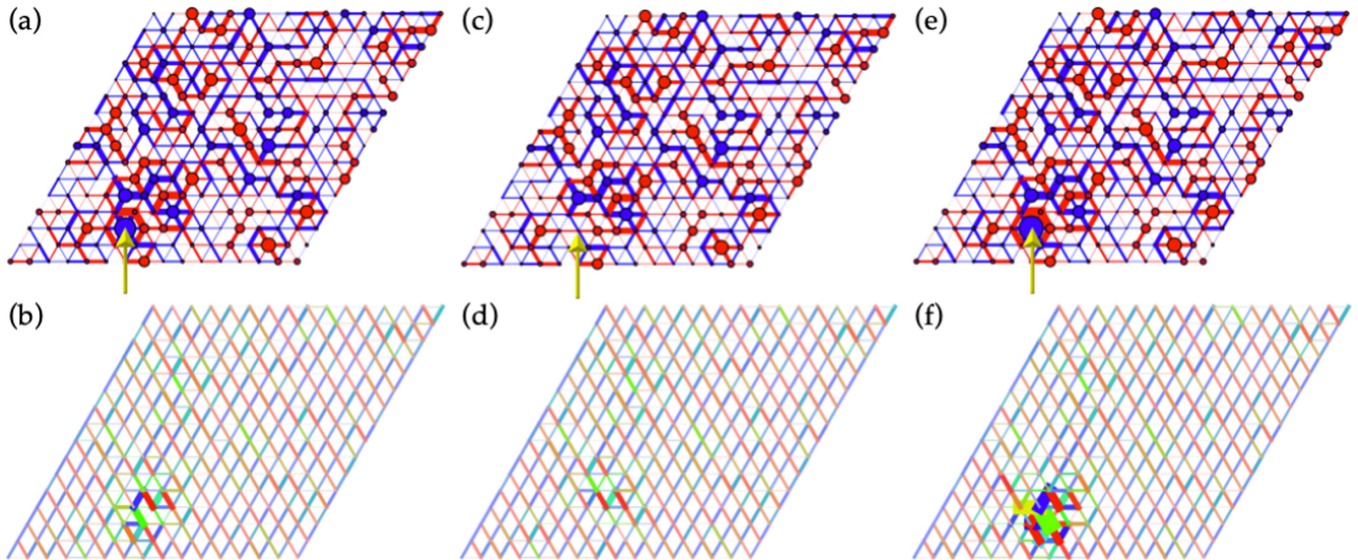


FIG. 2. Mechanical response of a nonconservative prestressed triangular lattice. (a) A triangular lattice with regular geometry and random, force-balanced, prestress (generated using the method described in Sec. III with $\bar{c} = 0.12$). Red and blue colors represent precompression and pretension on bonds and the thickness of the bond denote the magnitude of the prestress. (b) Response of the lattice in (a) under a shear load and periodic boundary conditions. The color scheme showing the increment of stress on each bond is defined in Fig. 4. (c) The same lattice as in (a) with the prestress on the most stressed site removed (corresponding to the particle on that site being damaged, releasing the stress, indicated by the yellow arrows), while keeping the lattice in force-balance. (d) Response of the lattice in (c) under the same shear load as in (b), displaying a more homogeneous response. (e) The same lattice as in (a) with the prestress on the most stressed sites carrying 15% more prestress (corresponding to the particle on the site actively respond to stress, growing when compressed, and shrinking when stretched), while keeping the lattice in force-balance. (f) Response of the lattice in (e) under the same shear load as in (b), displaying amplified heterogeneity.

distributions without detectable change in the geometry of the contact network [52,53], leading to drastically different, prestress-dependent, mechanical responses.

The fact that multiple microscopic stress distributions are compatible with the same macroscopic state of a particle or grains assembly, and that the same value of boundary stress corresponds to the so-called “force network ensemble” [52,54–56], is related to the broader concept of the “Edwards ensemble” [57] where both microscopic configuration and stress are allowed to vary for a given boundary stress. Statistical properties of prestress distributions in this type of ensembles have been recently discussed, and force-balance constraints [Eq. (1)] have been shown to produce intriguing long-range correlations [58–64]. Nevertheless, unraveling the role of disordered configurations and heterogeneous prestress in the mechanical response of these broad classes of amorphous solids has remained difficult both conceptually and computationally.

Here we present a systematic method to investigate how prestress affects the mechanical response of amorphous solids where the bond or contact configuration and the microscopic prestress are allowed to change *independently*, without assuming interactions are conservative. As we discuss below, prestress is a linear combination of the states of self stress (SSSs) of the stress-free version of the mechanical network, and leads to a new set of prestressed SSSs, capturing the unique, prestress-controlled, mechanical response of the system. By applying this method to a prestressed triangular lattice model with nonconservative bonds, we show how the change of prestress dramatically affects the mechanical response of

the system under load (Fig. 2). We also apply this method to a computational model of amorphous solids, showing how different preparation protocols lead to different patterns of prestress in the system, giving rise to significantly difference in their mechanical response, while the configuration shows little change (Fig. 3). The general method we introduce here is applicable to a wide range of systems, conservative or non-conservative, ordered and disordered, where prestress affects elasticity. It provides an efficient computational algorithm for finding the stress distribution when the system is under any load, as well as offering a platform to develop a field-theoretic treatment of prestressed elasticity of amorphous solids. Because this method allows the microstructure and the prestress field to vary separately in a nonconservative way, it offers a pathway to investigate how amorphous solids evolve as well as develop memory under stress without changing their bond or contact configuration, and potentially shed new light on the dynamical interplay between stress and geometry in these complex materials.

The paper is organized as follows. In Sec. II, we introduce a new formulation of equilibrium and compatibility matrices in prestressed networks, and discuss how they control both zero modes and stress response. In Sec. III, we use a prestressed triangular lattice model to illustrate how prestress controls the vibrational modes and the stress response and demonstrate how nonconservative interactions change the mechanical response of the system without any change in the geometry. In Sec. IV, we apply these methods to analyze the stress response of a computational model of prestressed amorphous solids, and Sec. V contains a summary and outlook.

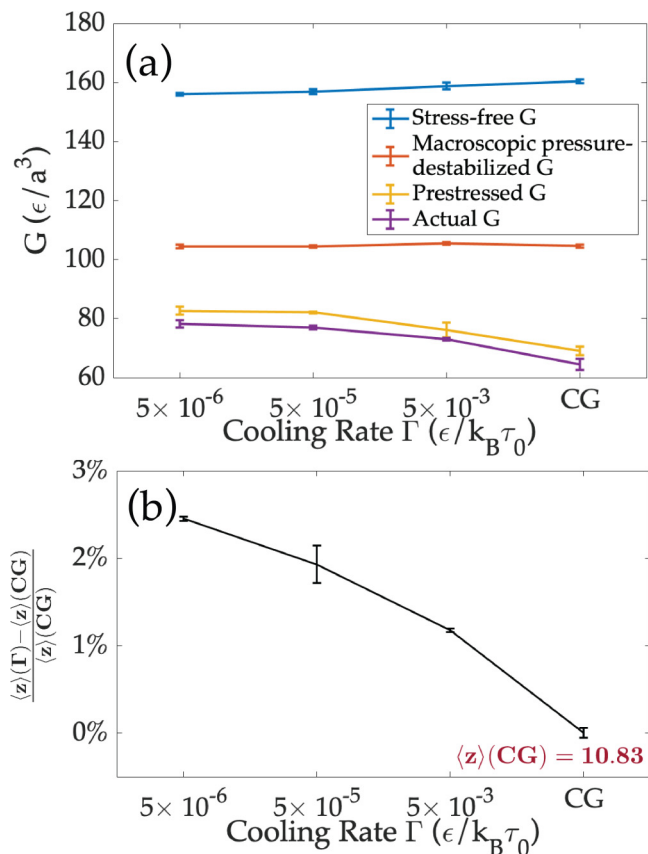


FIG. 3. Preparation protocol affects mechanics of three-dimensional prestressed amorphous solids at the same density (volume fraction $\phi \approx 70\%$). Details of the system and methods are discussed in Sec. IV. (a) Shear modulus drops by about 20% as the cooling rate increases, captured by our method including prestress (prestressed G). Dropping prestress in the computation (stress-free G) completely misses this effect. Destabilizing effect of the slight increase of pressure at higher cooling rate is far from enough (macroscopic pressure-destabilized G) in explaining this trend. (b) Real space configuration of the system, represented by the average coordination number $\langle z \rangle$ (which varied $<3\%$), remains almost the same, in accordance with the flat “stress-free” G curve.

II. PRESTRESSED MECHANICAL NETWORKS

In this section, we discuss fundamental principles of mechanics of prestressed networks in general conservative or nonconservative systems and how prestress affects their rigidity. We introduce a new \mathbb{Q}, \mathbb{C} (equilibrium and compatibility) matrices decomposition for the mechanics of these prestressed systems. We then use this formulation to discuss unique phenomena of zero modes (ZMs) and SSSs in prestressed systems, and analyze how they carry external load.

A. Prestressed mechanical networks

We consider a discrete network of point-like particles connected by pairwise interactions (bonds) which can be conservative or nonconservative. We start from a reference state where the position of particle ℓ is denoted by $\vec{R}_{\ell,0}$, and

consider a displacement field

$$\vec{R}_{\ell} = \vec{R}_{\ell,0} + \vec{u}_{\ell}. \quad (2)$$

The work done on a bond b connecting particles ℓ, ℓ' associated with this displacement field, δW_b , can be written as

$$\delta W_b = t_{b,p}(|\vec{R}_b| - |\vec{R}_{b,0}|) + \frac{k_b}{2}(|\vec{R}_b| - |\vec{R}_{b,0}|)^2, \quad (3)$$

where $t_{b,p}, k_b$ are the *pretension* and the spring constant of bond b , $\vec{R}_b \equiv \vec{R}_{\ell} - \vec{R}_{\ell'}$, and $\vec{R}_{b,0}$ is this vector in the reference state (which is not assumed to be stress-free). Defining $\vec{e}_b \equiv \vec{u}_{\ell} - \vec{u}_{\ell'}$ we can expand this form to quadratic order in \vec{u} as

$$\delta W_b = \frac{k_b}{2}|e_b^{\parallel}|^2 + \frac{t_{b,p}}{2|\vec{R}_{b,0}|}|e_b^{\perp}|^2, \quad (4)$$

where

$$e_b^{\parallel} \equiv \hat{R}_{b,0} \hat{R}_{b,0} \cdot \vec{e}_b, \quad e_b^{\perp} \equiv (\mathbb{I} - \hat{R}_{b,0} \hat{R}_{b,0}) \cdot \vec{e}_b \quad (5)$$

are components of \vec{e}_b parallel and perpendicular to the original bond direction $\hat{R}_{b,0} \equiv \vec{R}_{b,0}/|\vec{R}_{b,0}|$, respectively. A detailed derivation of this type for conservative systems can be found in Ref. [65].

It is worth noting that we don't require the system to be conservative. Here δW_b represents the work needed for the system to follow the displacement field \vec{u} . The spring constant k_b is allowed to change as a function of time and state, and the pretension $t_{b,p}$ does not need to be proportional to bond stretch from a certain “rest length.” In other words, δW_b is the infinitesimal work associated with the displacement field on a given initial state. This work is not necessarily stored in the system in the form as of elastic energy. A similar formalism has been utilized in Ref. [33] on active networks of cell sheets. We broadened this formulation to nonconservative interactions so it can be applied to problems such as dense suspensions and granular matter which involve complex frictional contacts.

When a network is prestressed, $t_{b,p} \neq 0$, both terms in Eq. (4) contribute to the work, increasing the number of microscopic constraints, as we discuss in detail in later parts of this section. Interestingly, in general the sign of $t_{b,p}$ can be either positive (tension) or negative (compression). In the case of $t_{b,p} > 0$, the prestress term contributes a complete square term to the work, clearly stabilizing the system. In the case of $t_{b,p} < 0$, naively, the prestress term appears to be unstable. However, because e_b^{\perp} are not variables independent of e_b^{\parallel} (of other bonds), the stability of the network needs to be analyzed in terms of the collective modes.

In addition, we assume that the network in the reference state is in *force balance*, i.e., the total force on each particle vanishes. As a result, there is no $\mathcal{O}(e)$ term in the expansion of the work. Note that *the force-balance condition and the stress-free condition are two distinct conditions*, where the later means $t_{b,p} = 0$ on all bonds, and is a much more stringent requirement than the force-balance condition.

B. States of self-stress in stress-free systems

In the rest of the section, we introduce the new \mathbb{Q}, \mathbb{C} decomposition for general conservative or nonconservative prestressed systems. We start by reviewing the \mathbb{Q}, \mathbb{C} decomposition in conservative stress-free systems already described in the literature [48,66,67] in this subsection. The elastic energy of a stress-free network of N pointlike particles connected by N_b central-force springs in d dimensions can be written to quadratic order in u using the dynamical matrix \mathbb{D}^{\parallel} as

$$E = \sum_{b=1}^{N_b} \delta V_b = \sum_{b=1}^{N_b} \frac{k_b}{2} (e_b^{\parallel})^2 = \frac{1}{2} \langle u | \mathbb{D}^{\parallel} | u \rangle, \quad (6)$$

where the inner product is taken in the Nd dimensional space for particle displacements u , and the superscript “ \parallel ” on the dynamical matrix signifies that this dynamical matrix describes a stress-free system where only e^{\parallel} enters the elastic energy. The more general form for prestressed systems will be discussed in Sec. II C. This quadratic form can be decomposed into two steps using the equilibrium and compatibility matrices, defined as

$$\mathbb{C}^{\parallel} | u \rangle = | e^{\parallel} \rangle, \quad (7)$$

$$\mathbb{Q}^{\parallel} | t^{\parallel} \rangle = - | f \rangle. \quad (8)$$

Here $| e^{\parallel} \rangle$ and $| t^{\parallel} \rangle$ represent the extension and tension of every bond, which are both N_b dimensional vectors, and the superscript “ \parallel ” indicated that they are along the bond direction. $| u \rangle$ and $| f \rangle$ represent the displacement and total force on every site, which are both Nd dimensional vectors. As a result, the equilibrium matrix \mathbb{Q} has the dimension $Nd \times N_b$, and the compatibility matrix \mathbb{C} has the dimension $N_b \times Nd$. The two matrices are in fact transpose of one another, $\mathbb{Q} = \mathbb{C}^T$. Note we take the convention that $t^{\parallel} > 0$ denotes tension and $t^{\parallel} < 0$ denotes compression. This is consistent with the minus sign of Eq. (8), as f is the force exerted by the bonds in the network on the sites.

Using these relations in Eq. (6), it is straightforward to see that

$$\mathbb{D}^{\parallel} = \mathbb{Q}^{\parallel} \cdot \mathbb{K}^{\parallel} \cdot \mathbb{C}^{\parallel}, \quad (9)$$

where \mathbb{K}^{\parallel} is a diagonal matrix that contains all the spring constants k_b . In the sign convention we use here, Hookian’s law on the springs takes the form $t^{\parallel} = \mathbb{K}^{\parallel} e^{\parallel}$, as extension causes tension on the springs.

The null space of \mathbb{Q}^{\parallel} is the set of tensions, called SSSs, that produce no forces at any site,

$$0 = \mathbb{Q}^{\parallel} | t_{\text{SSS}}^{\parallel} \rangle. \quad (10)$$

The null space of \mathbb{C}^{\parallel} is the set of site displacements, called ZMs, that produce no changes in bond lengths,

$$0 = \mathbb{C}^{\parallel} | u_{\text{ZM}} \rangle. \quad (11)$$

Floppy modes are a subset of ZMs excluding trivial rigid body motions of the whole system, and have been extensively studied in soft matter systems, due to their obvious significance as capturing deformations with no cost of elastic energy. SSSs have only recently been explored in soft matter but also show

great potential in characterizing stress-bearing structures in mechanical networks [68,69].

Applying rank-nullity theorem on \mathbb{Q}, \mathbb{C} matrices leads to the Maxwell-Calladine index theorem [67,70]

$$N_0 - N_S = Nd - N_b, \quad (12)$$

where N_0 and N_S are the numbers of ZMs and SSSs, respectively.

These concepts have found wide applications recently in the new field of topological mechanics, as $t_{\text{SSS}}^{\parallel}$ and u_{ZM} can become topologically protected modes in Maxwell lattices and networks [68,71–79].

C. States of self-stress in prestressed systems

Now we discuss the decomposition in prestressed systems which are not necessarily conservative. Firstly, the prestress itself can be viewed as “exciting” an existing SSS in the “stress-free version” of the same network (which is generated by turning off stress in the prestressed network but keeping exactly the same geometry),

$$\mathbb{Q}^{\parallel} | t_p \rangle = 0, \quad (13)$$

where \mathbb{Q}^{\parallel} is the equilibrium matrix of the stress-free version of the network, and the prestress is a SSS of this network. From this equation, it is clear that if \mathbb{Q}^{\parallel} has multiple SSSs, there are multiple ways to prestress the network. In a conservative system, the prestress t_p is uniquely determined by the configuration and the potential. In a nonconservative system, however, t_p can change as a result of micro and meso-scale processes, and a different SSS of the same \mathbb{Q}^{\parallel} can show up as the prestress. This may lead to interesting dynamical responses, which we discuss briefly in Sec. III using a lattice model.

Secondly, the work now includes both e_b^{\parallel} and e_b^{\perp} terms as analyzed in Eq. (4), and can be written in terms of a dynamical matrix as

$$\begin{aligned} W &= \sum_{b=1}^{N_b} \delta W_b = \sum_{b=1}^{N_b} \left[\frac{k_b}{2} (e_b^{\parallel})^2 + \frac{t_{b,p}}{2|\bar{R}_{b,0}|} |e_b^{\perp}|^2 \right] \\ &= \frac{1}{2} \langle u | (\mathbb{D}^{\parallel} + \mathbb{D}^{\perp}) | u \rangle. \end{aligned} \quad (14)$$

Similar to the stress-free case, using the fact that this work consists only of complete square terms, this dynamical matrix can also be decomposed into \mathbb{Q}, \mathbb{C} matrices,

$$\mathbb{D} = \mathbb{Q} \cdot \mathbb{K} \cdot \mathbb{C}, \quad (15)$$

where

$$\mathbb{C} | u \rangle = \begin{pmatrix} e^{\parallel} \\ e^{\perp} \end{pmatrix} \equiv | e \rangle, \quad (16)$$

defines the new \mathbb{C} matrix and $\mathbb{Q} = \mathbb{C}^T$. Here we have defined the new $N_b d$ dimensional e vector which contains one component from \parallel and $d - 1$ from \perp for each of the N_b bonds. It is worth noting here that the compatibility matrix \mathbb{C} is now $N_b d \times Nd$ dimensional instead of $N_b \times Nd$ dimensional, because this \mathbb{C} matrix maps the Nd dimensional displacement vector of the network into e_b^{\parallel} and e_b^{\perp} for each bond b . At the

same time, the equilibrium matrix \mathbb{Q} is $Nd \times N_b d$ dimensional. The spring constant matrix is a $N_b d \times N_b d$ diagonal matrix with spring constant k_b for the \parallel terms and pre-stress $t_{b,p}$ for the \perp terms,

$$\mathbb{K} = \begin{pmatrix} k_b & 0 \\ 0 & \frac{t_{b,p}}{|\bar{R}_{b,0}|} \end{pmatrix}, \quad (17)$$

where there are d blocks of N_b dimensional diagonal matrices (one longitudinal and $d - 1$ transverse).

These new \mathbb{Q} , \mathbb{C} matrices describe the mapping between the (Nd dimensional) degrees of freedom space and the (now $N_b d$ dimensional) constraint space. In parallel with Eq. (16), we have

$$\mathbb{Q} \begin{pmatrix} t^\parallel \\ t^\perp \end{pmatrix} \equiv \mathbb{Q}|t\rangle = -|f\rangle \quad (18)$$

Correspondingly, t^\parallel and t^\perp are the parallel and perpendicular components of t .

It might appear confusing how tension t on a central-force spring can have a component perpendicular to the spring. This can be understood by realizing that the \parallel and \perp components are defined with respect to the reference configuration, and t denotes an increment of stress in addition to the prestress t_p . In the prestressed reference state, $t_{b,p}$ is along bond b in the reference configuration $\bar{R}_{b,0}$. In the state after the (infinitesimal) deformation, the total tension is along bond b in the deformed configuration \bar{R}_b . These two bond directions, $\bar{R}_{b,0}$ and \bar{R}_b , are not parallel in general. The t field in Eq. (18) represents the increment from the pretension to the tension after the deformation, and thus has components parallel and perpendicular to the original bond direction. In other words, under an (infinitesimal) deformation, both bond (parallel) extension e^\parallel and bond rotation e^\perp cause increment of stress [Eq. (14)], and the two components are t^\parallel and t^\perp respectively.

SSSs in a prestressed system are thus defined as any vectors that satisfy

$$\mathbb{Q}|t_{\text{SSS}}\rangle = \mathbb{Q} \begin{pmatrix} t_{\text{SSS}}^\parallel \\ t_{\text{SSS}}^\perp \end{pmatrix} = -|f\rangle = 0, \quad (19)$$

which represent respectively parallel and perpendicular change of bond tensions that leave all particles in force balance, for a prestressed network. In Fig. 4, we show two examples of mechanical networks where prestress introduces extra SSSs that involve t^\perp components. This formulation characterizes the tensegrity phenomena [70,80] where prestress generates new SSSs for the system to carry other types of load.

D. Two types of zero modes in prestressed systems

Prestressed systems have two types of ZMs, type *A*, which leave $e^\parallel = e^\perp = 0$ on all bonds, and type *B*, which violate this relation but are still zero modes (defined as requiring no work in nonconservative systems). In this section we discuss both types of ZMs.

Type *A* ZMs in prestressed networks can be defined as modes that lie in the null space of \mathbb{C} ,

$$\mathbb{C}|u_{\text{ZM}}^{(A)}\rangle = \begin{pmatrix} e^\parallel \\ e^\perp \end{pmatrix} = |e\rangle = 0. \quad (20)$$

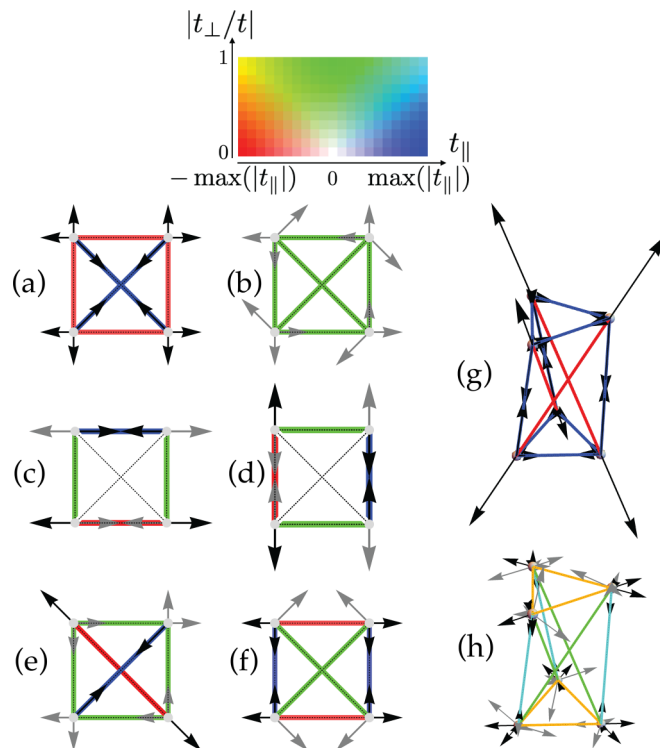


FIG. 4. Examples of SSSs in prestressed systems. (a) A stress-free mechanical network with one SSS. When the network is prestressed with this SSS, 5 new SSSs arise [(b)–(f)]. Bonds with t^\parallel , t^\perp in these SSSs are denoted by the color scheme shown on the top, where t^\parallel is denoted by red-white-blue as it goes from negative (compression) to positive (tension), and the relative strength of t^\perp over the total $t \equiv \sqrt{(t^\parallel)^2 + (t^\perp)^2}$ is denoted by green. The thickness of the bond is proportional to t , and the black (gray) arrows denote the component of t^\parallel , (t^\perp) on the nodes. (g) The tensegrity T3-prism has one SSS when it is stress-free. When it is prestressed with this SSS, 20 new SSSs arise, and one example of these SSSs is shown in (h). This example is chosen such that it carries the load of torsion between the top and bottom triangles (see Sec. II E for the projection of load onto SSSs).

The number of this type of ZMs satisfy the Maxwell-Calladine index theorem for a stressed network, which can be proven by applying the rank-nullity theorem on the new \mathbb{Q} , \mathbb{C} matrices,

$$N_0^{(A)} - N_S = Nd - N_b d. \quad (21)$$

Note that the last term is now $N_b d$ for the prestressed network instead of N_b in the stress-free case. More rigorously, if we also consider the possibility that not all bonds are stressed, this index theorem should be written as

$$N_0^{(A)} - N_S = Nd - N_b^{\text{unstressed}} - N_b^{\text{stressed}} d, \quad (22)$$

where each unstressed bonds only provide one constraint.

Type *B* ZMs in prestressed systems are not included in Eq. (20). Instead, they are ZMs due to the fact that some spring constants in \mathbb{K} are negative (from compressively prestressed bonds), and their contribution can cancel out the positive terms. They are “fine-tuning” ZMs which are only zero energy when the prestress satisfies certain conditions so that the positive and negative terms exactly cancel. One

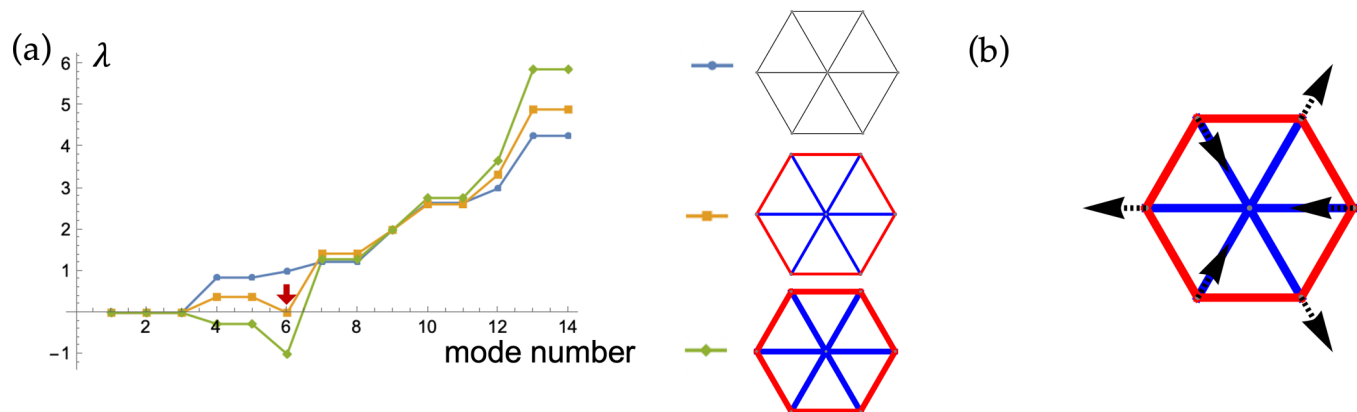


FIG. 5. Type B ZMs in prestressed systems. (a) Eigenvalues λ of the dynamical matrix of a mechanical network (right). When prestress on the network increase beyond a threshold, one normal mode becomes unstable (mode number 6 as shown by the red arrow), demonstrating an example of type B ZMs discussed in Sec. IID [black dashed arrows in (b)].

example of such mode is shown in Fig. 5. Interestingly, because $\mathbb{C}|u_{\text{ZM}}^{(B)}\rangle \neq 0$ and $\mathbb{Q}\mathbb{K}\mathbb{C}|u_{\text{ZM}}^{(B)}\rangle = 0$, type B ZMs lead to a set of SSSs $|t_{\text{SSS}}\rangle = \mathbb{K}\mathbb{C}|u_{\text{ZM}}^{(B)}\rangle$. One trivial example of this type of ZMs is the rigid rotation of the network if the system is under open boundary conditions: the rotation causes e^\perp and thus does not satisfy Eq. (20), but it is indeed a ZM of the dynamical matrix (this ZM does not require fine tuning of stress but all other type B ZMs do). A nontrivial example of such fine-tuning ZMs is shown in Fig. 5(e) where the sum of e^\parallel and e^\perp terms in the elastic energy vanish. Type B ZMs are not included in the Maxwell-Calladine index theorem for prestressed systems [Eq. (21)].

Remarkably, although ZMs in prestressed systems are more complicated as we discussed above, the definition of SSSs in Eq. (19) is robust as it relies only on force balance, and is not affected by the positive definiteness of \mathbb{D} . In our discussions below, we mainly focus on these SSSs and show how they form a linear space that efficiently characterizes how load is carried by a prestressed system.

E. Stress response to homogeneous load

One important property of SSSs is that they form a linear space containing *all* possible ways a network can carry stress while keeping all particles in force balance. Thus, when the network is under load, actual stress distributions must come from linear combinations of SSSs, and the linear space of SSSs characterizes the capability of a system to carry any external load. It is worth pointing out here that we refer to external loads that do not “introduce new constraints” to the system, and the meaning of this condition will become clear at the end of Sec. III F.

Here we first illustrate this formulation using a simple shear on a stress-free network with all spring constants being 1. The bond tension in response to this shear can be decomposed in the SSSs linear space because this space form a complete basis for all force-balanced stress distributions, as we discussed above. The decomposition can be written as

$$|t^\parallel\rangle = \sum_{i=1}^{N_{\text{SSS}}} |t_{\text{SSS},i}^\parallel\rangle \langle t_{\text{SSS},i}^\parallel | e_{\text{affine}}^\parallel \rangle, \quad (23)$$

where $e_{\text{affine}}^\parallel$ is the bond extension if the strain were affine (i.e., homogeneous shear strain). The sum runs in the N_{SSS} dimensional linear space of all SSSs, $|t_{\text{SSS},i}^\parallel\rangle$. This relation is straightforward to prove as follows: when a strain is imposed on the system (e.g., via Lees-Edwards boundary conditions in a computational model, or in the bulk of a mechanical network strained from the boundary), in addition to affine bond extensions $e_{\text{affine}}^\parallel$, the system responds by particle displacements u (e.g., nonaffine deformations) to minimize the elastic energy while maintaining this macroscopic strain, so the resulting bond extensions are

$$|e^\parallel\rangle = |e_{\text{affine}}^\parallel\rangle + \mathbb{C}^\parallel |u\rangle. \quad (24)$$

If all spring constants are 1, we have $|t^\parallel\rangle = |e^\parallel\rangle$. As we mentioned above, $|t^\parallel\rangle$ must belong to the SSSs linear space, and the linear combination coefficients are

$$c_i = \langle t_{\text{SSS},i}^\parallel | t^\parallel \rangle = \langle t_{\text{SSS},i}^\parallel | e_{\text{affine}}^\parallel \rangle + \langle t_{\text{SSS},i}^\parallel | \mathbb{C}^\parallel |u\rangle. \quad (25)$$

The second term has to vanish because $\langle t_{\text{SSS},i}^\parallel | \mathbb{C}^\parallel = (\mathbb{Q}^\parallel |t_{\text{SSS},i}^\parallel\rangle)^T = 0$. This proves the decomposition in Eq. (23).

Three comments can be made from this result. First, if the shear strain has no overlap with any SSSs in the system, $\langle t_{\text{SSS},i}^\parallel | e_{\text{affine}}^\parallel \rangle = 0$ for all i , the system can not carry the load. What would happen physically is that the system yields until a new SSS, able to carry that load, emerges. Second, the same approach can also be applied to other types of load, such as a hydrostatic pressure. It is important to note here that any component in the imposed strain that can be written in terms of $\mathbb{C}^\parallel |u\rangle$ will not cause stress—it corresponds to strain that will be relaxed by degrees of freedom available to the system. Third, a similar formulation can also be developed with loads applied via specifically controlled boundary displacements, where SSSs are defined as bond tensions leaving internal sites in force balance, and the strain e can be applied from bonds connected to boundaries [73].

The relation is slightly more complicated when the spring constants are different for each spring,

$$|t^\parallel\rangle = \sum_{i,j} |t_{\text{SSS},i}^\parallel\rangle [(\mathbb{K}^\parallel)^{-1}]_{ss}^{-1} \langle t_{\text{SSS},j}^\parallel | e_{\text{affine}}^\parallel \rangle, \quad (26)$$

where $((\mathbb{K}^{\parallel})^{-1})_{ss}$ is the inverse of the spring constant matrix projected to the SSS linear space (see detailed definition in Appendix A).

Equation (26) only assumes a linear relation between infinitesimal bond extensions and tensions, and does not require the interactions to be conservative, so it can readily be generalized to the prestressed and nonconservative case, where

$$|t\rangle = \sum_{i,j}^{N_{\text{SSS}}} |t_{\text{SSS},i}\rangle [(\mathbb{K}^{-1})_{ss}]^{-1} \langle t_{\text{SSS},j} | e_{\text{affine}} \rangle. \quad (27)$$

A detailed proof of this relation is included in Appendix A. It is worth noting that the response $|t\rangle$ calculated here is the addition to the prestress in response to the load, so the total stress in the system is $|t_p\rangle + |t\rangle$ where t_p only has longitudinal components and t has both longitudinal and transverse components (with respect to the bond direction in the prestressed reference state).

F. Stress response to force dipoles

Similar projections can also be applied to compute the stress response of a prestressed system to local forces, such as a force dipole acting on a bond.

The main difference between this case of a force dipole and the external strain case discussed in Sec. II E is that the force-balance condition here needs to include the external forces,

$$\mathbb{Q}|t_{\text{rsp}}\rangle = -|f_{\text{rsp}}\rangle = |f_{\text{external}}\rangle \quad (28)$$

where f_{external} is the externally imposed force and t_{rsp} is the tension response of the system, which causes f_{rsp} . f_{rsp} cancels with f_{external} , leaving the system in force balance.

When the external forces take the form of a force dipole on a bond b , they can be written as

$$|f_{\text{external}}\rangle = |f_{\text{dipole}}\rangle = -\mathbb{Q}|t_{\text{dipole}}\rangle = -\mathbb{Q}\mathbb{K}|b\rangle \quad (29)$$

where $|b\rangle$ is a vector in the bond space with 1 on the bond where the dipole is imposed, and 0 on all other bonds. This sets the magnitude of the dipole force to be $k_b \cdot 1$, the value of which is irrelevant for the linear theory. The sign convention of this equation follows from Eq. (18) where t_{dipole} causes f_{dipole} . Combining Eqs. (28) and (29), we have

$$\mathbb{Q}(|t_{\text{dipole}}\rangle + |t_{\text{rsp}}\rangle) = 0, \quad (30)$$

indicating that the total tension field $t_{\text{dipole}} + t_{\text{rsp}}$ (sum of the external dipole and the network response) is a SSSs of the network. The response can then be derived using a similar method as discussed in Sec. II E, and we have (as detailed in Appendix B)

$$|t_{\text{rsp}}\rangle = -|t_{\text{dipole}}\rangle + \sum_{i,j}^{N_{\text{SSS}}} |t_{\text{SSS},i}\rangle [(\mathbb{K}^{-1})_{ss}]_{ij}^{-1} \langle t_{\text{SSS},j} | b \rangle. \quad (31)$$

In the simple case of $\mathbb{K} = k\mathbb{I}$ (all springs having the same spring constant which only applies to stress-free networks), the second term on the right hand side of the equation reduces to the “quasi-localized SSSs” defined in the stress-free case, characterizing dipole responses [69,81]. Here we extend this concept to prestressed networks, and our formulation can be used to not only compute dipoles with force along the bond,

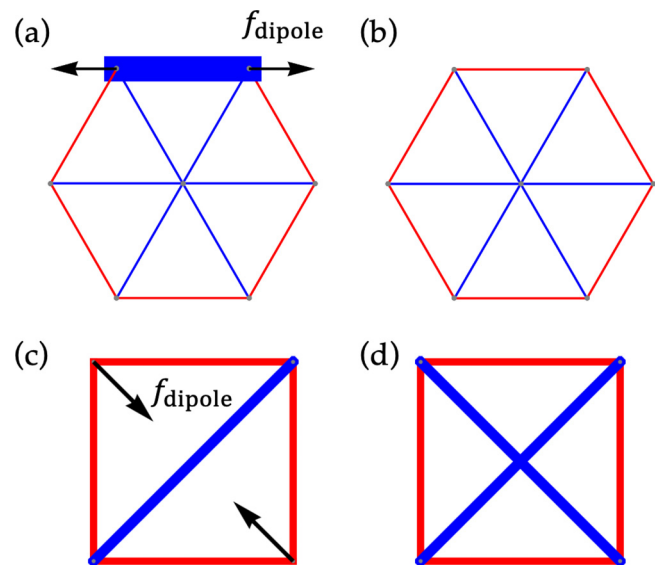


FIG. 6. Stress response to dipole forces. (a) Bond stress response of a mechanical network to a force dipole f_{dipole} (black arrows) acting on a bond in the network. Blue and red marks the tension $t_{\text{rsp}} > 0$ and compression $t_{\text{rsp}} < 0$ on the bonds in response to the force dipole, with the thickness of the bond proportional to the magnitude of the tension/compression. (b) The sum of the external dipole and the network response, $t_{\text{dipole}} + t_{\text{rsp}}$, is a SSS of the network. (c) Bond stress response of a mechanical network to a force dipole acting on a pair of particles not connected by a bond. This force dipole can be viewed as an additional bond in the network, such that $t_{\text{dipole}} + t_{\text{rsp}}$ is a SSS of the network with the added bond (d). The original structure in (c) does not have any SSS.

but also “transverse” or “tilted” dipoles where the force pair is perpendicular or in an arbitrary angle to the bond (see example in Fig. 6).

A “dipole stiffness” κ can then be defined to characterize this response

$$\kappa \equiv \frac{\langle f_{\text{dipole}} | f_{\text{dipole}} \rangle}{\langle f_{\text{dipole}} | u_{\text{rsp}} \rangle}, \quad (32)$$

where $\langle f_{\text{dipole}} |$ serves the purpose of projecting the force and displacements to the direction of the external force dipole. A different version of (longitudinal only) dipole stiffness has been introduced in Ref. [82] where u_{rsp} of the whole system is used instead of its projection to the dipole was used. In contrast, the dipole stiffness defined here treats the whole system as a black box, and only extracts the stiffness from the force-distance relation between the two particles where the dipole acts on. The simplicity of this definition allows it to be directly implemented in experiments via methods such as microrheology.

Using the SSSs linear space, the dipole stiffness to a local force dipole on bond b is thus given by (details in Appendix B):

$$\kappa_b = \frac{2k_b^2}{k_b - \sum_{i,j}^{N_{\text{SSS}}} \langle b | t_{\text{SSS},i} \rangle [(\mathbb{K}^{-1})_{ss}]^{-1} \langle t_{\text{SSS},j} | b \rangle}, \quad (33)$$

where k_b is the spring stiffness for bond b .

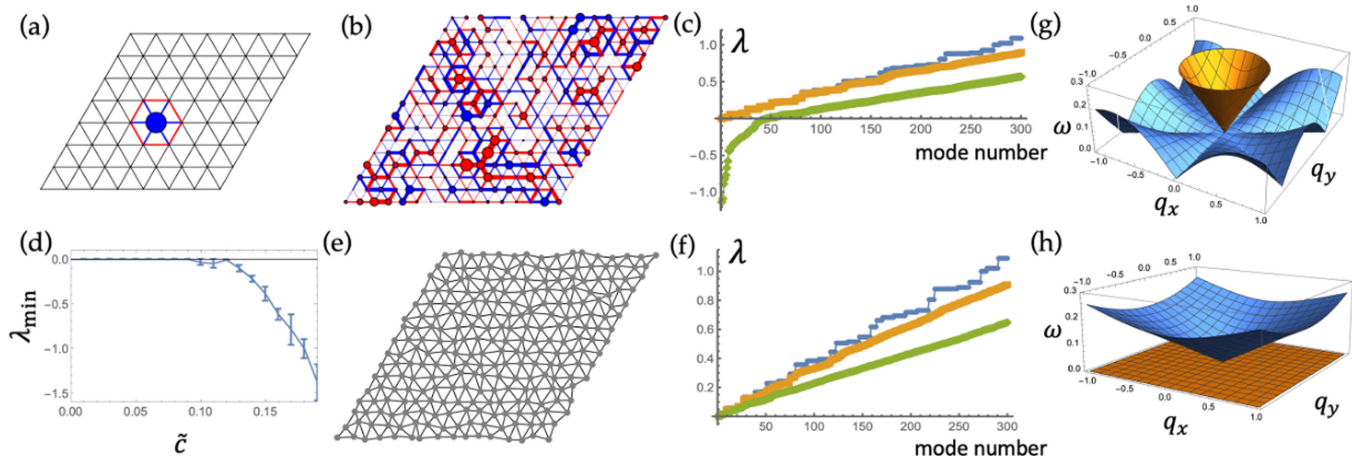


FIG. 7. Vibrational modes of prestressed triangular lattices. (a) One site-localized SSS $|t_\ell\rangle$ on a triangular lattice, where bonds surrounding the hexagon carry compression, and bonds in the hexagon carry tension. The size of the blue disk on the center site represents the strength of this SSS. (b) A prestressed triangular lattice with the prestress t_p generated using a linear combination of site-localized SSSs with independent coefficients on each site, drawing from a Gaussian distribution with mean 0 and standard deviation $\tilde{c} = 0.12$. (c) Lowest 300 eigenvalues λ of the dynamical matrix of prestressed triangular lattices of size 32×32 , at $\tilde{c} = 0$ (blue), 0.1 (orange), and 0.2 (green), from top to bottom. (d) The lowest eigenvalue λ_{\min} as a function of \tilde{c} . (e) A triangular lattice with positional disorder where the random displacements of the nodes have standard deviation $\tilde{u} = 0.12$. (f) Lowest 300 eigenvalues λ of the dynamical matrix of a 32×32 triangular lattices with positional disorder, at $\tilde{u} = 0$ (blue), 0.1 (orange), and 0.2 (green), from top to bottom. (g) Phonon dispersion relation of the lowest band of triangular lattices with no prestress (yellow, top) and critical compressive prestress (blue, bottom) where modes along ΓM approach instability. (h) Phonon dispersion relation of the lowest band of honeycomb lattices with no prestress (yellow, bottom) and positive tension (blue, top).

Another interesting case of force dipole is when the dipole acts on a pair of particles that are not connected in the network (which can be called “nonlocal dipoles”). The analysis of force-balance in this case can be done by considering the external force dipole as *introducing an additional constraint into the network*. Thus, the stress distribution is a SSS of the network with this additional “auxiliary bond,” instead of the original network. In Appendix B, we also derive the dipole stiffness of this case. Examples of both types of dipoles are shown in Fig. 6.

III. PRESTRESSED ELASTICITY OF TRIANGULAR LATTICES

In this section, we use prestressed triangular lattices to illustrate the mathematical tools for prestressed elasticity we discussed in Secs. II. Models of prestressed triangular lattices have been introduced in the literature of force network ensembles, as an example system where multiple internal stress distributions are compatible with given boundary stress [52,54,55]. Here we discuss how our SSSs formulation can be applied to these lattices to both systematically generate all possible prestress distributions, and solve for vibrational modes and stress response to external load, revealing interesting prestress effects.

In the stress-free case, triangular lattices have a coordination number $z = 6 > 2d$ and thus the number of SSSs per site is $\frac{z}{2} - 2 = 1$. In fact, a localized SSS $|t_\ell\rangle$ can be defined around each site ℓ as shown in Fig. 7(a). These site-localized SSSs, together with the homogeneously state of self stress (all bonds carrying the same tension), form a complete basis to decompose any SSSs on the triangular lattice. A similar construction of prestress states on Delaunay triangulations has

been developed in Ref. [83] to characterize rigidity in granular solids. In particular, we can generate an ensemble of prestress $|t_p\rangle$ on triangular lattices by taking an arbitrary coefficient c_ℓ for each site-localized SSS $|t_\ell\rangle$ and sum them up. In Fig. 7(b), we show an example of such a prestressed state.

One way to physically construct these prestressed triangular lattices is to choose the rest length of each bond b such that when they are at the length in the regular triangular lattice, the tension/compression they carry is exactly the value $t_{b,p}$ in the prescribed SSSs. Because the total force is balanced at each site for any SSS, all bonds will stay at the length in the regular lattice, and thus we obtain a triangular lattice with *regular geometry and a prescribed SSS*. On the other hand, when the interactions are nonconservative, one is allowed to choose any value for the pretension on each bond. As long as the total force on all sites vanish, the system is still in force balance.

What are the mechanical properties of such prestressed triangular lattices? Here we study them from two perspectives: vibrational modes and load-bearing capabilities. The vibrational modes can be calculated based on the quadratic expansion in Eq. (4) for each bond, which leads to the dynamical matrix defined in Eq. (15).

In Fig. 7(c), we show eigenvalues of the dynamical matrix of the triangular lattice at three levels of prestress (by assigning c_ℓ from a Gaussian distribution with mean at 0 and standard deviation at \tilde{c}). Prestress significantly affects the vibrational modes especially at low frequencies. In particular, negative eigenvalues start to appear when the fluctuations of the SSSs goes beyond a critical level, $\tilde{c} > \tilde{c}^*$ [Figs. 7(c) and 7(d)]. This indicates that by increasing the fluctuation of prestress (where the mean remains 0), unstable modes appear, although the system remains in force balance. This is in

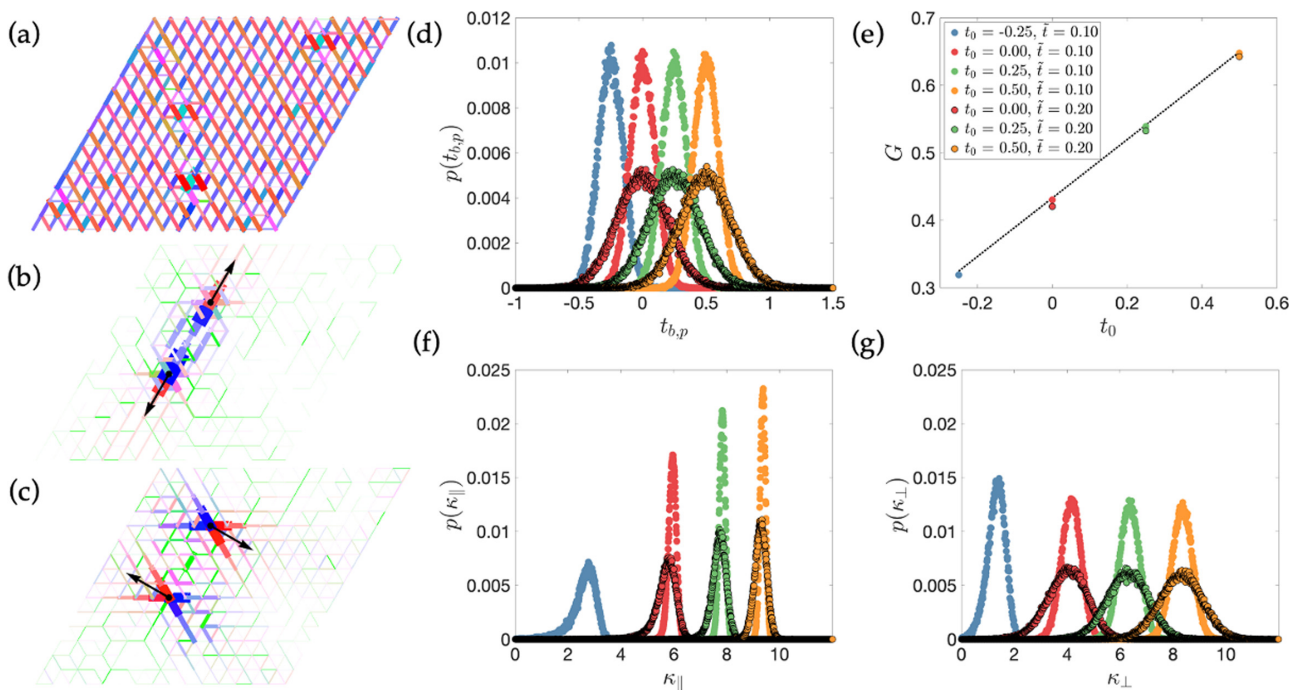


FIG. 8. Prestressed triangular lattices under load. [(a)–(c)] An example of a prestressed triangular lattice [the one shown in Fig. 7(b)] under shear load ϵ_{xy} (a), a longitudinal dipole (b), and a transverse dipole (c), where the force dipoles are shown as black arrows. The color scheme of bond tensions (t^{\parallel} and t^{\perp}) is the same as in Fig. 4. (d) Probability distributions of pretensions on bonds of the lattices we tested for load bearing, with different mean t_0 and standard deviation \tilde{t} of pretension on bonds [legend shown as inset of (e)]. (e) Shear modulus G of these lattices as a function of mean pretension t_0 . [(f)–(g)] Probability distributions of the parallel (f) and transverse (g) local dipole stiffness of these lattices. 20×20 lattices are used in the computations in (d)–(g), and we average over 100 realizations of disorder for each set of parameters.

alignment with our discussion on prestressed rigidity and type B ZMs of prestressed systems in Sec. II.

To contrast this result, we also consider triangular lattices with positional disorder but no prestress [Fig. 7(e)]. In this case, we move site ℓ by a random displacement \tilde{u}_{ℓ} , the x , y components of which being generated from a Gaussian distribution with mean at 0 and standard deviation at \tilde{u} . We also plot the eigenvalues of the dynamical matrix of this case in Fig. 7(f). Although positional disorder also affects the eigenvalues, it mostly smooths out the regular lattice eigenmodes, and does not lead to qualitative change at low frequencies and does not generate unstable modes. Note that to make a fair comparison we chose the same values for \tilde{c} and \tilde{u} , which represents the same level of disorder, under the simple convention we took where the bond length and spring constant on the triangular lattice both being unity.

The load-bearing capabilities of prestressed triangular lattices can be analyzed by the SSSs formalism discussed in Sec. II. At any given realization of disordered prestress, we can compute the linear space of SSSs, and use Eqs. (27) and (31) to find the stress response of the system to external load [Figs. 8(a)–8(c)]. In particular, to characterize the homogeneous component of prestress (hydrostatic pressure), we also introduce a constant pretension t_0 on all bonds, in addition to the fluctuations from $\langle t_{\ell} \rangle$. As a result, the tension on each bond obeys a normal distribution with mean at t_0 and standard deviation at $\tilde{t} = 2\tilde{c}$ (as each bond appears in four site-localized SSSs around it), as shown in Fig. 8(d). We apply two types of load, simple shear and dipole forces, on these prestressed triangular lattices, and the results are shown in

Fig. 8. This analysis shows that for both shear modulus and stiffness against dipole forces, their mean is mainly controlled by t_0 (where compression decreases stiffness and tension increases stiffness, in qualitative agreement with Ref. [84] where effects of prestress is characterized in a mean-field approximation) whereas \tilde{t} slightly decreases these stiffness, as well as broadens them. In addition, the stress response demonstrates interesting heterogeneities due to the disordered prestress, an effect we will discuss more in Sec. IV.

Effects of prestress on mechanics can also be seen from the perspective of phonon structures of regular lattices [Figs. 7(g) and 7(h)]. It is straightforward to see that negative prestress (compression) destabilizes the originally stable triangular lattice [Fig. 7(g)] and positive prestress (tension) stabilizes the honeycomb lattice [Fig. 7(h)], which was originally unstable against shear. Interestingly, the modes that first become unstable in the triangular lattice as negative prestress increase are the modes along the ΓM direction in the first Brillouin zone, indicating that the type of modes that first become unstable are the modes that zigzag between the straight lines of bonds, agreeing with recent studies of strain localization in lattice models [85].

When nonconservative dynamics is introduced to the system, the lattice displays dramatically different mechanical response even when the configuration is kept the same. In Fig. 2 we show two cases as examples: (i) when the most stressed particle “crush” and release its stress, and (ii) when the most stressed particle experiences some active increases of its stress, mimicking, e.g., positive feedback in biomechanical systems. These effects provide interesting new topics

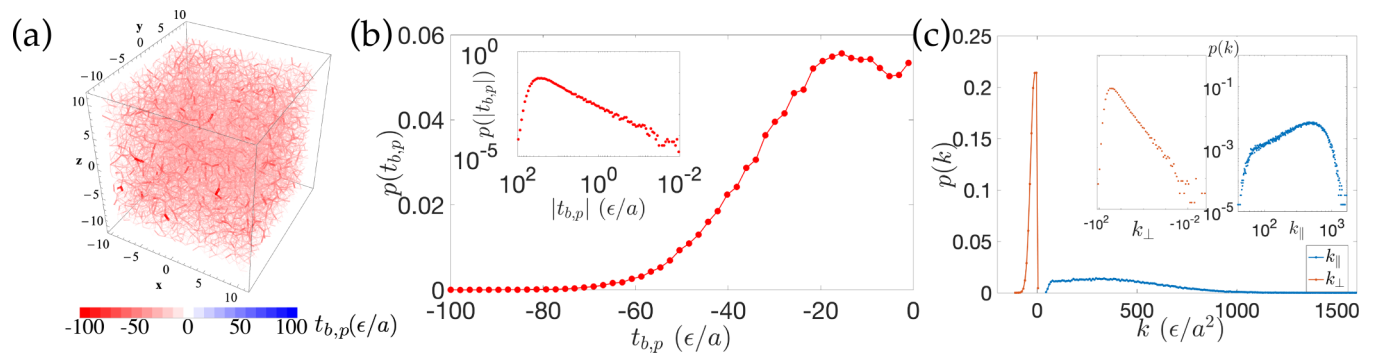


FIG. 9. Prestress in amorphous solids of repulsive particles. (a) Pretension on bonds $t_{b,p} \equiv \frac{dU(r_{ij})}{dr_{ij}}$ where b is the bond connecting particles i, j . The system size is $N = 10976$ with preparation cooling rate $\Gamma = 5 \times 10^{-6} \epsilon / (k_B \tau_0)$. [(b) and (c)] Distributions of $t_{b,p}$ (b), and spring constants $k_{||} \equiv k_b$ and $k_{\perp} \equiv \frac{t_{b,p}}{|\hat{R}_{b,0}|}$ (c), for the configuration shown in (a).

for future studies of dynamical nonconservative mechanics in amorphous solids.

IV. PRESTRESSED ELASTICITY OF AMORPHOUS SOLIDS OF SOFT REPULSIVE PARTICLES

The new \mathbb{Q}, \mathbb{C} matrix approach described in Sec. II provides a set of tools to analyze stress-bearing capabilities and mode structures of prestressed systems well beyond the triangular lattices just described. Here we apply this method to a computational model for amorphous solids composed of soft repulsive particles, where, akin to real materials, prestresses are naturally introduced by the preparation (solidification) protocol. Given the preparation protocol chosen for this study, the prestress is the result of both compression and frozen-in structural disorder.

A. 3D numerical simulations of amorphous solids of soft repulsive particles

The numerical model describes a suspension of particles with soft repulsive interactions given by a truncated and shifted Lennard-Jones potential [86]. The potential energy, for a pair of two particles ℓ and ℓ' separated by a center-to-center distance $R_b \equiv |\hat{R}_{\ell} - \hat{R}_{\ell'}|$, is $V(R_b) = 4\epsilon[(a_b/R_b)^{12} - (a_b/R_b)^6] + \epsilon$ for particle pairs closer than the cutoff distance $R_b \leq r_c \equiv 2^{1/6}a_b$, otherwise $V(R_b) = 0$, following the notation we defined in Sec. II. Here $a_b = (a_{\ell} + a_{\ell'})/2$ with a_{ℓ} and $a_{\ell'}$ being the diameters. The size polydispersity is introduced by drawing the diameter of each particle a_i from a Gaussian distribution with mean a and variance of 10%. The parameter ϵ is the unit energy and a is the unit length in the simulations. Particles closer than the cutoff distance (beyond which the inter-particle force vanishes), $R_b \leq r_c$, are considered in contact. All simulations used here have volume fraction $\phi \approx 70\%$ and consist of 10^4 (10976) particles in a cubic box of linear size $L = 20.36$, unless otherwise specified. The initial samples are prepared by first melting face-centered-cubic (FCC) crystals of particle at volume fraction 0.7 at $T = 5.0\epsilon/k_B$. We then cool the particle assemblies down to a temperature $0.001\epsilon/k_B$ through an NVT molecular dynamics (MD) protocol as described in Ref. [87]. The cooling rate Γ varies from 5×10^{-2} to $5 \times 10^{-6} \epsilon / (k_B \tau_0)$, where $\tau_0 = a\sqrt{m/\epsilon}$ is the MD

time unit with m the particle mass. Subsequently, each sample is brought to the closest local energy minimum using a conjugate gradient (CG) algorithm. The configurations prepared in this way are amorphous solids, as we verify by measuring their viscoelastic response [87], whose properties depend on the cooling rate utilized. These solids feature prestress that comes both from the homogeneous compression and from the structural disorder due to the size polydispersity.

In Fig. 9, we show a typical configuration where prestress on the bonds are visualized. These $t_{b,p}$ terms are negative as the system is compressed. For each cooling rate, we prepare 5 statistically independent samples. All quantities investigated here have been averaged over this set of samples and we obtain error bars from sample to sample fluctuations.

We examine these samples as they are sheared using Lees-Edwards boundary conditions and a shear rate $\dot{\gamma}$, by solving Newton equations of motions with a drag force that guarantees minimal inertia effects as discussed in Ref. [87]. All simulations are performed with LAMMPS [88], suitably modified to include the particle size polydispersity and the interactions discussed above, and using a shear rate $\dot{\gamma} = 10^{-4}\tau_0^{-1}$. We also perform quasistatic shear deformations to characterize the mechanical response of the system, and confirm that the results at the lowest strain rate and the quasistatic test are consistent.

With the bond network and particle coordinates, we build the compatibility and equilibrium matrices \mathbb{Q} and \mathbb{C} , to study the prestressed elasticity using the general formalism described in the previous sections. In this 3D network, each bond has one longitudinal $t^{||}$ and two transverse directions t^{\perp} for tension increments. We take the convention that the first transverse direction $\hat{R}_{b,0}^{\perp,1} \equiv \hat{R}_{b,0} \times \hat{z} / |\hat{R}_{b,0} \times \hat{z}|$ is the unit vector of the cross product between the bond unit vector $\hat{R}_{b,0}$ and the z axis (0,0,1), and the second transverse direction $\hat{R}_{b,0}^{\perp,2} \equiv \hat{R}_{b,0} \times \hat{R}_{b,0}^{\perp,1}$ is the unit vector of the cross product between the bond vector and the first transverse direction [the subscript 0 signifies the reference (undeformed but prestressed) state].

Once the \mathbb{Q} and \mathbb{C} matrices are constructed, we solve their null space and obtain ZMs and SSSs of the computational model. The samples we studied are in general deep in the solid phase and exhibit no ZMs besides the three trivial translations. When solving for SSSs in large and dense systems

as the samples we generated, the null space for the equilibrium matrix \mathbb{Q} may have very high dimensions. We used the SPQR_RANK package [89] from SUITESPARSE [90], which is a high performance sparse QR decomposition package and can provide a reliable determination of null space basis vectors for large sparse matrices, to solve for SSSs efficiently and reliably, especially when there are lots of degeneracies for diagonalizing \mathbb{Q} . Similarly, SPQR_RANK is also suitable when solving for the null space of \mathbb{Q}^T to get ZMs in large systems.

Compared to computational methods currently being used to study prestressed mechanical networks, where singular value decomposition (SVD) is applied to the dynamical matrix, leading to expensive computations, our new method based on the equilibrium matrix greatly improves the efficiency. By decomposing the dynamical matrix, $\mathbb{D} = \mathbb{Q}\mathbb{C}$, we exploit the intrinsic sparsity of the problem, which allows the more efficient high performance sparse QR decomposition methods.

B. Calculating stress response to shear using prestressed states of self-stress

We begin by demonstrating the power of the SSSs as “stress-eigenstates” that characterize the stress-bearing capabilities of a prestressed system. To this end, we compute all SSSs as described above, and use Eq. (27) to calculate the change of tension, t^\parallel and t^\perp , as the system is under macroscopic shear, which we call “prestressed response” here, as this is the difference between the stress under load and the prestress.

To contrast this result, we also calculated the tension increment treating the system as a stress-free network, i.e., as characterized by equilibrium matrix \mathbb{Q}^\parallel instead of \mathbb{Q} (where the geometry of the contact network is kept the same). The resulting stress increment (which only has the t^\parallel component) is then calculated using Eq. (26), and we will call this the “stress-free response.” At the same time, we also measure the change of the stress in the system in a numerical experiment where the system is under a small shear deformation imposed quasistatic or at finite rate (as specified in captions of Figs. 10 and 11), and we call this the “actual response.”

In the next two sections, we compare these different results on tension increment in terms of both spatial heterogeneity and shear modulus.

C. Spatial heterogeneity of stress response

One significant effect of prestress on the mechanical response of amorphous solids is the spatial heterogeneity of the stress increment, in contrast to the stress-free response (where the geometry is kept the same). Figure 10 shows a visualization of the tension increment in the model amorphous solids we study here.

Remarkably, this heterogeneity is accurately depicted from the SSSs calculation when prestress is included. The tension increment is computed following Eq. (27). The resulting t field includes both t^\parallel and t^\perp , although only t^\parallel is shown. To be precise, t^\perp manifests as rotations of the bonds in the real response (which causes the total tension to change direction). In contrast, the calculated stress response of the system

ignoring the prestress effect, i.e., using Eq. (26), is almost completely homogeneous. Thus, in these dense systems, *the prestress controls the spatial heterogeneity of the mechanical response of the system*. Treating the system as “stress-free” misses important signatures of heterogeneities.

We characterize the spatial heterogeneity of the tension increment using a clustering tendency index: the Hopkins statistic H [91], with a value close to 1 indicating the data are highly clustered, and a value around 0.5 from random data. Figure 10(c) shows that the prestressed elasticity captures the tension increment clustering tendency which exists in real tension responses, while in stress-free elasticity this clustering is not captured.

D. Shear modulus of prestressed amorphous solids

The shear modulus G can be obtained from the shear component of the virial stress [87]. All components of the virial stress can be obtained from the SSSs projection calculation (which directly gives t_b^\parallel, t_b^\perp of all bonds b) via

$$\vec{t}_b = (t_{b,p} + t_b^\parallel)\hat{R}_{b,0}^\parallel + t_b^{\perp,1}\hat{R}_{b,0}^{\perp,1} + t_b^{\perp,2}\hat{R}_{b,0}^{\perp,2}, \quad (34)$$

$$\vec{R}_b = \left(R_{b,R} + \frac{|\vec{t}_b|}{k_b} \right) \hat{t}_b, \quad (35)$$

where $\hat{t}_b \equiv \vec{t}_b/|\vec{t}_b|$ is the direction of the bond after the deformation.

E. Effect of cooling rate on stress response

By varying the cooling rate as described above, we prepare particle assemblies that have different amount of disorder and compressive prestress, and have shown elsewhere that the higher cooling rates lead to a higher degree of disorder, characterized through a Voronoi analysis of the local particle packing which shows a decrease in the local icosahedral order [19,87].

The total number of SSSs in a prestressed system N_S is directly related to the numbers of degrees of freedom and constraints via the Maxwell-Calladine index theorem [Eq. (21)] as the system exhibits no ZMs except for the trivial translations. In Fig. 12(a), we show the total number of SSSs in different configurations of our model amorphous solid that were prepared by varying the cooling rate. The number N_S decreases with the increase of cooling rate. Figures 12(b) and 12(c) show that this effect is accompanied by a decrease in the number of bonds and a net increase of the average compressional prestress. These findings support the idea that varying the preparation protocol by varying the cooling rate, as we do, induces different amount of prestress into amorphous solid configurations, which can be directly captured by the SSSs analysis. The data also indicate that more aged samples, which tend to be stiffer, feature larger amounts of SSSs.

This is consistent with the finding in Ref. [19] that more aged samples (i.e., prepared with a lower cooling rate) contained larger amounts of (overconstrained) icosahedrally packed domains, identified through the Voronoi analysis of the particle packing. These domains, which tend to be stiffer, were shown to favor the accumulation of stress and promote dilation when the samples were driven towards yielding under

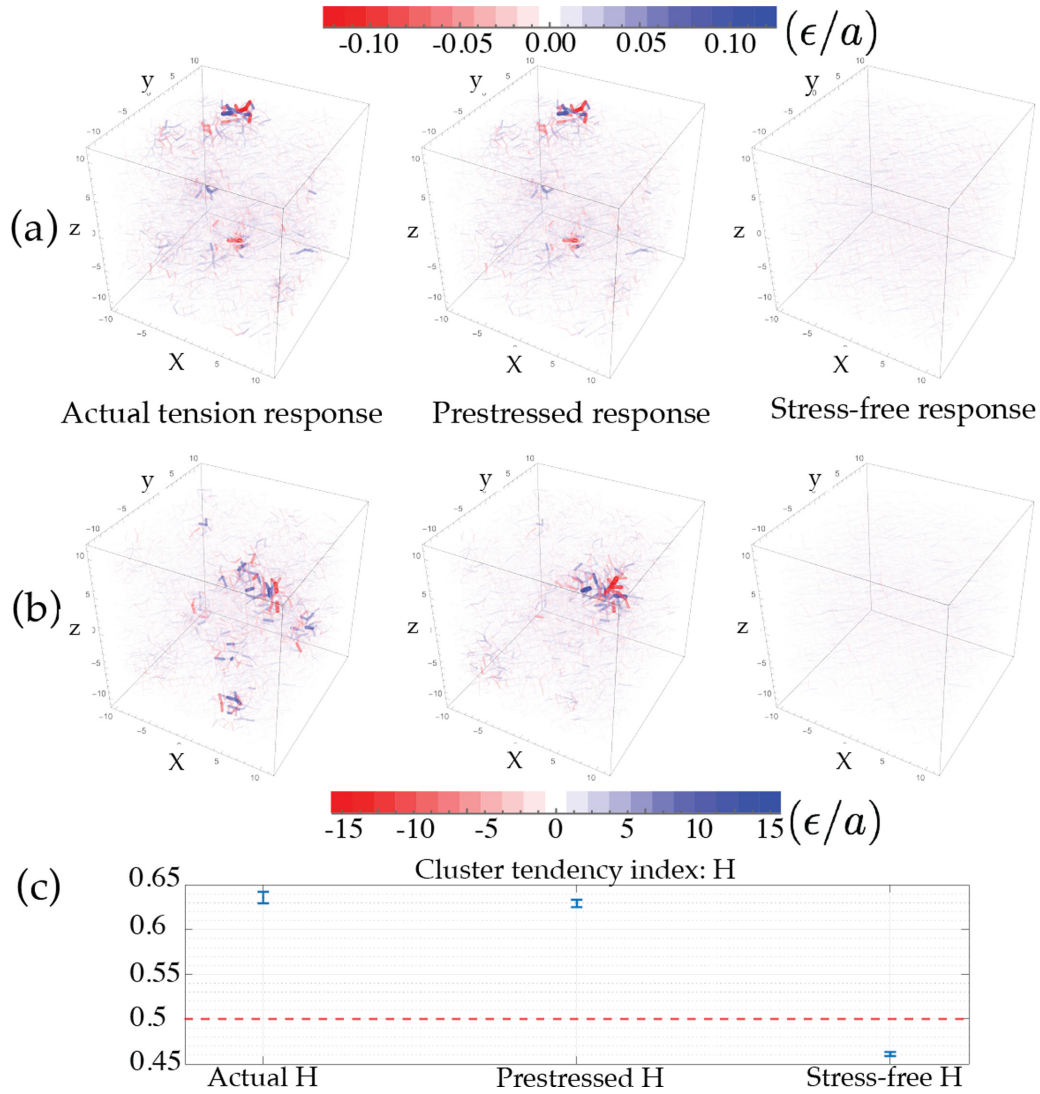


FIG. 10. Spatial heterogeneity of tension increment of prestressed networks under shear strain. We compare the actual tension response t measured in simulation to the tension increment calculated with and without prestress, for a quasistatic shear deformation at strain 0.01% in (a) and a finite rate shear deformation at strain 1% in (b) (system size $N = 10976$ and cooling rate $\Gamma = 5 \times 10^{-2} \epsilon / (k_B \tau_0)$). (c) Clustering tendency index H averaged over three different samples calculated using stress-free and prestressed elasticity compared to the actual H measured at quasistatic shear strain 0.01%. The red dashed line indicates the threshold to determine whether or not the tension change is clustered.

a shear deformation. The comparison of the results obtained here with the analysis performed in Refs. [19,87] support the idea that those phenomena, i.e., the increase in stiffness and in the tendency to accumulate stress and dilate under shear, should be due to prestress, and that sizable changes in the number of SSSs, as a result of sizable differences in prestress, eventually determine sizable changes in the linear, and even nonlinear, response of amorphous solids.

We also study the effect of cooling rate on the shear modulus (Fig. 3). As we discussed above, cooling rate controls prestress, and this in turn causes the shear modulus G to significant decrease with increasing cooling rate. The method we introduce here accurately captures this trend, which would be completely missed if the system was treated as stress-free. Interestingly, this is not just due to the destabilizing effect of the increasing pressure p . It is known that pressure

decreases shear rigidity, since $G = K_{xyxy} + \sigma_{p,yy}$ where K is the stress-free elastic moduli matrix and $\sigma_{p,yy} = -p$ is the compressional prestress [1]. However this effect alone cannot explain the decreasing trend of G with decreasing cooling rate. Our analysis reveals that this decrease originates from local prestresses encoded in the intricate and frustrated geometries of the dense packing of particles, rather than from a global hydrostatic pressure.

F. Dipole stiffness in prestressed glasses

SSSs have been also discussed in the context of the mechanical response of amorphous solids to local perturbations (e.g., force dipoles), which could be connected to the localized or quasi-localized plastic processes that are key ingredients of the mechanical response of this class of materials [69,81]. The

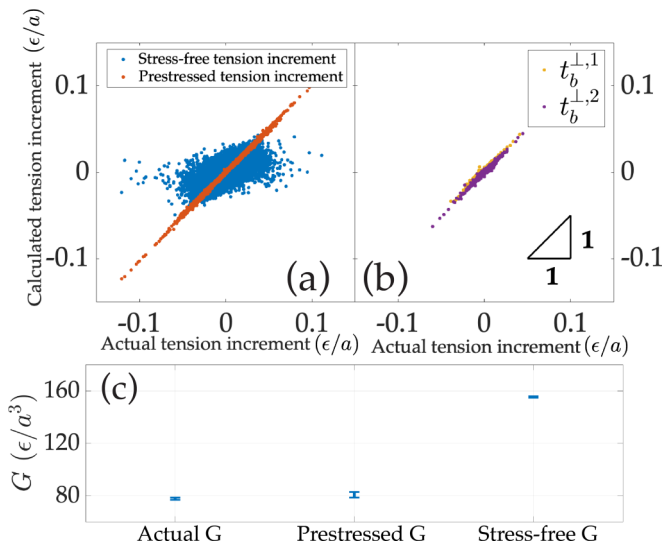


FIG. 11. Comparing tension increment calculated from SSSs projection and numerical experiments (actual tension) of quasistatic 0.01% shear strain [system size $N = 10976$ and cooling rate $\Gamma = 5 \times 10^{-6} \epsilon / (k_B \tau_0)$]. [(a) and (b)] Comparison of calculated and actual tension increment (t^{\parallel}, t^{\perp}) of each bond, where good agreement is found in the case of prestressed formulation. (c) Shear modulus G from stress-free response and prestressed response compared to the actual G . The shear modulus is averaged over three different configurations at quasistatic 0.01% shear strain, with the same system size and preparation protocol to the system in (a) and (b).

analysis of nonaffine and plastic microscopic displacements under shear and of their spatial correlations has led to the notion of “soft spot,” i.e., the presence of localized regions that are especially susceptible to plastic rearrangements under an external force [43,47,92–94].

The local response to force dipoles that we have discussed in Sec. II F has been directly related to these soft spots in

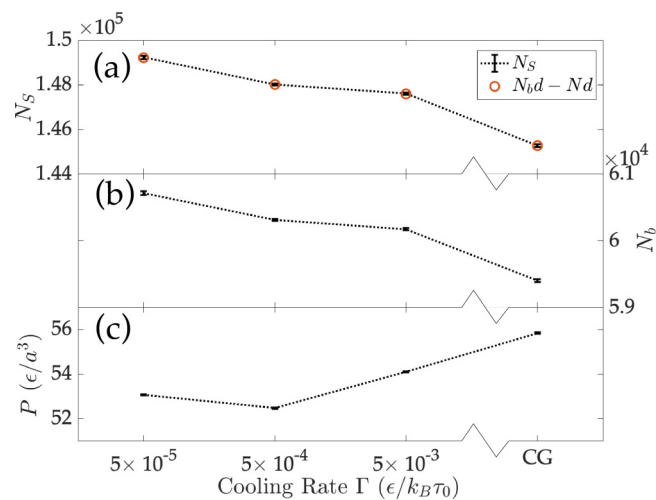


FIG. 12. Statistics of SSSs at different cooling rate. (a) Number of SSSs (N_s), (b) number of bonds (N_b), and (c) averaged normal stress (P) for different cooling rates Γ . Those quantities are averaged over five different configurations for each cooling rate, and the system size is $N = 10976$.

amorphous solids [69,81,95] and such response analysis has pointed to quasilocalized excitations (QLEs). In general, one needs to follow the time evolution of a system under an external deformation to identify the QLEs, however similar characteristics have been extracted, in the case of model glasses and amorphous solids, even in the low-frequency limit of the vibrational spectrum, i.e., from the linear response regime [43,47,49,94].

Here we use the newly developed methods to examine the response of the model amorphous solids obtained in simulations to dipole forces, and collect the statistics of the local stiffness these systems display. In particular, we apply the approach for force dipoles discussed in Sec. II F, and calculate the stiffness as defined in Eq. (32) for each bond, to identify regions which are soft. Measures of this kind lend themselves, in fact, to identify soft regions with respect to various external perturbations.

Interestingly, the relative displacement that a pair of particles undergoes during a plastic rearrangement is typically not along the direction of the bond that initially connects them. Instead, this local deformation involves several sliding motions. Therefore a particularly interesting measure of local softness, potentially complementing recently proposed ones [27,81,96], can be obtained by quantifying the stiffness against a dipole, whose forces are along a different direction from the one of the bond on which they are applied. Thus, for each bond, in addition to computing the dipole stiffness to longitudinal (along t^{\parallel}) and transverse (along t^{\perp}) forces, we compute the softest dipole stiffness, κ_b^{\min} , by minimizing it with respect to the direction of the dipole forces (details in Appendix B).

Figure 13(a) shows an example of applying longitudinal and transverse force dipoles on a bond in our prestressed particle configurations, showing both \parallel and \perp tension responses of all bonds. Remarkably, although the near field response is mainly in the \parallel direction, the far field response contains significant t^{\perp} components. This is a genuine effect of prestress—these transverse stress response can only be captured when prestress is included.

We collect the statistics of the minimum dipole stiffness κ_b^{\min} on bonds in the networks obtained with two different preparation cooling rates as shown in Fig. 13(g). These distributions feature a power-law tail for small κ_b^{\min} , where $p(\kappa_b^{\min}) \sim (\kappa_b^{\min})^{\beta}$ and β appears to depend on the cooling rate. The results demonstrate the impact of preparation history to the mechanical stiffness in prestressed systems. The case with faster cooling rate leads to a smaller exponent and thus the distribution extends more to soft κ_b^{\min} , agreeing with the general trend discussed in Sec. IV E, where faster cooling rate leaves more heterogeneities regarding stress response in the sample. Our results also provide an interesting comparison to (longitudinal) dipole stiffness distributions studied in Ref. [82] for different models of computational glasses.

Furthermore, we also characterize the spatial distribution of κ_b^{\min} and compare it to the spatial distribution of prestress $t_{b,p}$ [Figs. 13(h) and 13(i)]. Remarkably, κ_b^{\min} shows interesting spatial patterns whose possible correlations with the amount of prestress in these regions are however hard to tease out. Relating regions with clustered soft κ_b^{\min} with soft spots will be an interesting question for future studies.

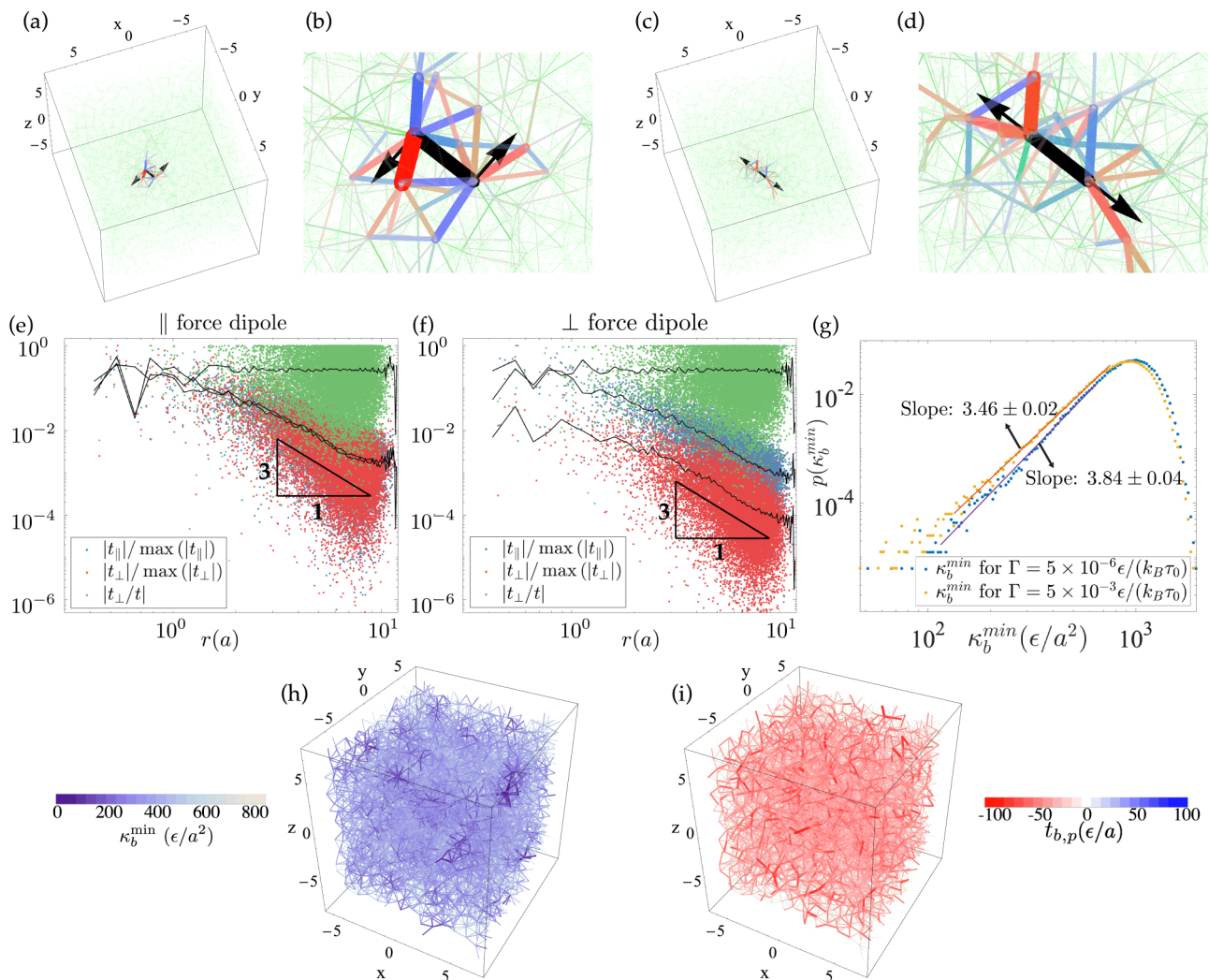


FIG. 13. Dipole responses in amorphous solids. [(a)–(d)] Tension responses to a transverse (a) or longitudinal (c) force dipole applied on the a bond (black arrows). The color scheme showing t^{\parallel} , t^{\perp} is the same as the one used in Fig. 4. (b) and (d) are zoomed-in views near the bond in (a) and (c) respectively. [(e) and (f)] Spatial decay of tension responses for the two force dipoles in (a) and (c) respectively. (g) Distribution of minimum dipole stiffness κ_b^{\min} for systems with different preparation cooling rates. System size is $N = 2916$. The distribution is averaged over 10 samples for each cooling rate. (h) Spatial distribution of κ_b^{\min} on bonds for a configuration of system size $N = 2916$ and preparation cooling rate $\Gamma = 5 \times 10^{-6} \epsilon / (k_B \tau_0)$. Bonds with soft κ_b^{\min} are thicker and more opaque. (i) Pretension $t_{b,p}$ on bonds for the same configuration in (h).

V. DISCUSSION

Through this paper, we have developed a set of mathematical tools to investigate elasticity of prestressed discrete networks, which allows prestress to vary independently from the bond or contact configuration, which is particularly important for nonconservative systems, offering new insight into the mechanical response of amorphous solids and other prestressed structures such as tensegrity metamaterials and robotics.

Our method starts from the geometry of a mechanical network. By temporarily treating it as stress-free, we can calculate the self stress the network can carry. The prestress lies in the linear space formed by all states of self stress of the stress-free network [Eq. (13)]. While the actual prestress in a conservative system is uniquely determined by the interaction potentials and the geometry, the prestress in

nonconservative systems can change—as long as it stays in this linear space—without breaking force balance or changing the configuration of the network. We then introduce a new equilibrium-compatibility matrix decomposition for the network with prestress, without assuming conservative mechanics, which can be conveniently and efficiently used to compute the mechanical response of the prestressed network.

In particular, we not only characterize how prestress affects vibrational modes, both stabilizing soft modes and introducing a new class of ZMs (type *B*, which appear due to competing positive and negative terms in the energy), but also reveal its profound role on how the mechanical network carries additional stress. By analyzing prestressed SSSs of the network, and projecting external load to this linear space, our methods conveniently map how external stress transmits in prestressed lattices and bond networks obtained from model amorphous solids. We show a number of intriguing effects

which are unique to prestressed networks, including the spatial heterogeneity in the stress-response to homogeneous loads even far from the rigidity transition, the power-law distribution of the local stiffness and the isotropic nature of the long-range stress response to local perturbations such as force dipoles. In particular, our formulation allows the calculation of responses to transverse dipoles, typically associated to microscopic rearrangements in amorphous solids. Moreover, we show how nonconservative evolution of prestress can greatly change the mechanical response of the network in intriguing ways.

The ability to conveniently characterize mechanical response of nonconservative systems of our theory offers a new perspective to analyze the dynamics of amorphous solids under strain. In real amorphous solids, from granular matter to colloids, particle-particle interactions are not simple harmonic springs. Instead, they evolve under stress in non-conservative and often unpredictable ways—microfracturing, crushing, sintering. This evolution is further complicated by the role of the solvent, where contacts between particles can be lubricated or frictional. Therefore *stress distributions can significantly change with little change in the configuration*. Our methods provide a convenient set of tools to examine how the mechanical response of these amorphous materials may evolve as the system explores an ensemble of states where only internal stress is changed.

Prestress records the preparation history in amorphous solids and has an important role in directing the mechanical response beyond the linear regime. The implications of prestress and preparation history, in fact, have been highlighted with respect to the development of flow inhomogeneities upon yielding [19] and in connection with the fundamental physics mechanisms controlling brittle or ductile yielding phenomena [18,20,51]. Our methods, therefore, have wider relevance as they can be applied beyond the linear response to investigate, through the SSSs characteristics, the role of prestress in plasticity and yielding. The new tools discussed here can potentially close the feedback loop between structure and stress, opening a new pathway to study how amorphous solids yield and solidify under external strain.

Finally, friction plays a central role in the complex behaviors of exotic rigid states emerging in granular matter and dense suspensions, leading to fascinating phenomena from shear jamming to discontinuous shear thickening [5,97–102]. Interestingly, friction also lives in the t^\perp channel of stress, and a linear relation with e^\perp can also be assumed, hence it would be a natural next step to include friction into the SSSs description. However, the Coulomb threshold imposes an upper limit to t^\perp that is not part of the methods developed here. How the frictional and the prestress contributions to t^\perp interplay and affect the macroscopic dynamics of the material, will be of great interest for future studies.

ACKNOWLEDGMENTS

This work is supported in part by the National Science Foundation under Grant No. NSF-DMR-2026825 (X.M.), NSF-DMR-2026842 (E.D.G), NSF-EFRI-1741618 (S.Z., L.Z., and X.M.), and the Office of Naval Research under Grant No. MURI N00014-20-1-2479 (E.S. and X.M.).

APPENDIX A: SSSs FORMULATION FOR SHEAR RESPONSE OF PRESTRESSED NETWORKS

1. Projection of a shear load to the SSSs linear space

When a mechanical network is subject to a shear load, the resulting bond extensions and rotations can be written as the sum of contributions from the affine shear field e_{affine} and the nonaffine displacements $\mathbb{C}|u_{\text{rsp}}\rangle$,

$$|e\rangle = |e_{\text{affine}}\rangle + \mathbb{C}|u_{\text{rsp}}\rangle, \quad (\text{A1})$$

which is similar to Eq. (24) in the main text, but here we include both the parallel and the perpendicular components of e .

When force-balance is reached, net force on each particle vanishes,

$$-|f\rangle = \mathbb{Q}|t\rangle = \mathbb{Q}(\mathbb{K}(|e_{\text{affine}}\rangle + \mathbb{C}|u_{\text{rsp}}\rangle)) = 0. \quad (\text{A2})$$

This means that $|t\rangle = \mathbb{K}(|e_{\text{affine}}\rangle + \mathbb{C}|u_{\text{rsp}}\rangle)$ must be a vector that belongs to the null space of \mathbb{Q} . Thus it can be written as a linear combination of the SSSs of the system.

To facilitate the discussion of this SSSs linear combination, we define the following notations. Let $\{\tilde{t}_s^{(1)}, \dots, \tilde{t}_s^{(N_s)}\}$ be an orthonormal basis of the null space of \mathbb{Q} , and let P_s^Q denote the $N_{bd} \times N_s$ matrix whose columns are $\tilde{t}_s^{(1)}, \dots, \tilde{t}_s^{(N_s)}$, i.e., $P_s^Q = [\tilde{t}_s^{(1)}, \dots, \tilde{t}_s^{(N_s)}]$. One can also define the $N_{bd} \times (N_{bd} - N_s)$ dimensional matrix P_r^Q whose columns are an orthonormal basis of the orthogonal complement of the null space of \mathbb{Q} . Similarly, one can define the $Nd \times N_0$ matrix P_s^C whose columns are an orthonormal basis of the null space of \mathbb{C} (ZMs), and the $Nd \times (Nd - N_0)$ matrix P_r^C whose columns are an orthonormal basis of the orthogonal complement of the null space of \mathbb{C} . These matrices are represented as

$$P_s^Q = [\tilde{t}_s^{(1)}, \dots, \tilde{t}_s^{(N_s)}], \quad (\text{A3})$$

$$P_r^Q = [\tilde{t}_r^{(1)}, \dots, \tilde{t}_r^{(N_{bd}-N_s)}], \quad (\text{A4})$$

$$P_s^C = [\tilde{u}_s^{(1)}, \dots, \tilde{u}_s^{(N_0)}], \quad (\text{A5})$$

$$P_r^C = [\tilde{u}_r^{(1)}, \dots, \tilde{u}_r^{(Nd-N_0)}], \quad (\text{A6})$$

and they satisfy the following identities:

$$(P_s^Q)^T \cdot P_s^Q = \mathbb{I}_{(N_s)}, \quad (\text{A7})$$

$$(P_r^Q)^T \cdot P_r^Q = \mathbb{I}_{(N_{bd}-N_s)}, \quad (\text{A8})$$

$$(P_s^C)^T \cdot P_s^C = \mathbb{I}_{(N_0)}, \quad (\text{A9})$$

$$(P_r^C)^T \cdot P_r^C = \mathbb{I}_{(Nd-N_0)}, \quad (\text{A10})$$

$$P_s^Q \cdot (P_s^Q)^T + P_r^Q \cdot (P_r^Q)^T = \mathbb{I}_{(N_{bd})}, \quad (\text{A11})$$

$$P_s^C \cdot (P_s^C)^T + P_r^C \cdot (P_r^C)^T = \mathbb{I}_{(Nd)}, \quad (\text{A12})$$

where $\mathbb{I}_{(N_s)}$ is an identity matrix of dimension N_s , and other definitions follows similarly.

As we discussed above, $|t\rangle$ is a linear combination of the SSSs,

$$|t\rangle = \sum_i^{N_s} \alpha_i |t_{\text{SSS},i}\rangle = P_s^Q \cdot \tilde{\alpha}, \quad (\text{A13})$$

where $\vec{\alpha}$ are coefficients of the linear combination of $|t\rangle$ as the SSSs.

Because the basis we use are orthonormal,

$$\vec{\alpha} = (P_s^Q)^T |t\rangle = (P_s^Q)^T \mathbb{K}(|e_{\text{affine}}\rangle + \mathbb{C}|u_{\text{rsp}}\rangle), \quad (\text{A14})$$

$$\vec{0} = (P_r^Q)^T |t\rangle = (P_r^Q)^T \mathbb{K}(|e_{\text{affine}}\rangle + \mathbb{C}|u_{\text{rsp}}\rangle), \quad (\text{A15})$$

inserting identity matrix [Eq. (A11)] into Eq. (A15) and using the fact that

$$\mathbb{Q} \cdot P_s^Q = \vec{0},$$

we have

$$\begin{aligned} \vec{0} &= (P_r^Q)^T \mathbb{K} \cdot [P_s^Q \cdot (P_s^Q)^T + P_r^Q \cdot (P_r^Q)^T] \cdot (|e_{\text{affine}}\rangle + \mathbb{C}|u_{\text{rsp}}\rangle) \\ &= (P_r^Q)^T \mathbb{K} \cdot [P_s^Q \cdot (P_s^Q)^T \cdot \mathbb{Q}^T + P_r^Q \cdot (P_r^Q)^T \cdot \mathbb{Q}^T] \cdot |u_{\text{rsp}}\rangle \\ &\quad + (P_r^Q)^T \mathbb{K} \cdot [P_s^Q \cdot (P_s^Q)^T + P_r^Q \cdot (P_r^Q)^T] \cdot |e_{\text{affine}}\rangle \\ &= (P_r^Q)^T \mathbb{K} \cdot P_r^Q \cdot (P_r^Q)^T \cdot \mathbb{Q}^T \cdot |u_{\text{rsp}}\rangle + (P_r^Q)^T \mathbb{K} \\ &\quad \cdot [P_s^Q \cdot (P_s^Q)^T + P_r^Q \cdot (P_r^Q)^T] \cdot |e_{\text{affine}}\rangle \\ &= \mathbb{K}_{rr} (P_r^Q)^T \mathbb{Q}^T \cdot |u_{\text{rsp}}\rangle + [\mathbb{K}_{rs} (P_s^Q)^T + \mathbb{K}_{rr} (P_r^Q)^T] \cdot |e_{\text{affine}}\rangle \\ &\Rightarrow (P_r^Q)^T \mathbb{Q}^T \cdot |u_{\text{rsp}}\rangle \\ &= -(\mathbb{K}_{rr})^{-1} [\mathbb{K}_{rs} (P_s^Q)^T + \mathbb{K}_{rr} (P_r^Q)^T] \cdot |e_{\text{affine}}\rangle, \quad (\text{A16}) \end{aligned}$$

where we defined the decomposition of \mathbb{K} into the null and orthogonal compliment space as

$$\mathbb{K} \rightarrow \begin{pmatrix} (P_s^Q)^T \cdot \mathbb{K} \cdot P_s^Q & (P_s^Q)^T \cdot \mathbb{K} \cdot P_r^Q \\ (P_r^Q)^T \cdot \mathbb{K} \cdot P_s^Q & (P_r^Q)^T \cdot \mathbb{K} \cdot P_r^Q \end{pmatrix} = \begin{pmatrix} \mathbb{K}_{ss} & \mathbb{K}_{sr} \\ \mathbb{K}_{rs} & \mathbb{K}_{rr} \end{pmatrix} \quad (\text{A17})$$

and also used the fact that \mathbb{K}_{rr} is invertible.

The coefficients $\vec{\alpha}$ in Eq. (A14) can then be solved as

$$\begin{aligned} \vec{\alpha} &= (P_s^Q)^T \mathbb{K} \cdot [P_s^Q \cdot (P_s^Q)^T + P_r^Q \cdot (P_r^Q)^T] \\ &\quad \cdot (\mathbb{Q}^T |u_{\text{rsp}}\rangle + |e_{\text{affine}}\rangle) \\ &= (P_s^Q)^T \mathbb{K} \cdot P_r^Q \cdot (P_r^Q)^T \cdot \mathbb{Q}^T \cdot |u_{\text{rsp}}\rangle \\ &\quad + (P_s^Q)^T \mathbb{K} \cdot [P_s^Q \cdot (P_s^Q)^T + P_r^Q \cdot (P_r^Q)^T] \cdot |e_{\text{affine}}\rangle \\ &= \mathbb{K}_{sr} (P_r^Q)^T \mathbb{Q}^T \cdot |u_{\text{rsp}}\rangle \\ &\quad + [\mathbb{K}_{ss} (P_s^Q)^T + \mathbb{K}_{sr} (P_r^Q)^T] \cdot |e_{\text{affine}}\rangle. \end{aligned}$$

Plug in Eq. (A16) to eliminate u_{rsp} ,

$$\begin{aligned} \vec{\alpha} &= \mathbb{K}_{sr} \{ -(\mathbb{K}_{rr})^{-1} [\mathbb{K}_{rs} (P_s^Q)^T + \mathbb{K}_{rr} (P_r^Q)^T] \cdot |e_{\text{affine}}\rangle \} \\ &\quad + [\mathbb{K}_{ss} (P_s^Q)^T + \mathbb{K}_{sr} (P_r^Q)^T] \cdot |e_{\text{affine}}\rangle \\ &= \{ \mathbb{K}_{sr} (P_r^Q)^T + \mathbb{K}_{ss} (P_s^Q)^T - \mathbb{K}_{sr} (\mathbb{K}_{rr})^{-1} \\ &\quad \times [\mathbb{K}_{rs} (P_s^Q)^T + \mathbb{K}_{rr} (P_r^Q)^T] \} \cdot |e_{\text{affine}}\rangle \\ &= [\mathbb{K}_{ss} (P_s^Q)^T - \mathbb{K}_{sr} (\mathbb{K}_{rr})^{-1} \mathbb{K}_{rs} (P_s^Q)^T] \cdot |e_{\text{affine}}\rangle \\ &= [\mathbb{K}_{ss} - \mathbb{K}_{sr} (\mathbb{K}_{rr})^{-1} \mathbb{K}_{rs}] \cdot (P_s^Q)^T \cdot |e_{\text{affine}}\rangle. \quad (\text{A18}) \end{aligned}$$

This can be further simplified by letting $\mathbb{A} = \mathbb{K}^{-1}$ and decompose \mathbb{A} into the column-space and null-space of \mathbb{Q} as

$$\mathbb{A} \rightarrow \begin{pmatrix} (P_s^Q)^T \cdot \mathbb{A} \cdot P_s^Q & (P_s^Q)^T \cdot \mathbb{A} \cdot P_r^Q \\ (P_r^Q)^T \cdot \mathbb{A} \cdot P_s^Q & (P_r^Q)^T \cdot \mathbb{A} \cdot P_r^Q \end{pmatrix} = \begin{pmatrix} \mathbb{A}_{ss} & \mathbb{A}_{sr} \\ \mathbb{A}_{rs} & \mathbb{A}_{rr} \end{pmatrix}. \quad (\text{A19})$$

One can see that

$$\mathbb{K}_{ss} \cdot \mathbb{A}_{ss} + \mathbb{K}_{sr} \cdot \mathbb{A}_{rs} = \mathbb{I}_{ss}, \quad (\text{A20})$$

$$\mathbb{K}_{rs} \cdot \mathbb{A}_{ss} + \mathbb{K}_{rr} \cdot \mathbb{A}_{rs} = \vec{0}_{rs}. \quad (\text{A21})$$

Right multiply by $(\mathbb{A}_{ss})^{-1}$ on both sides of two equations:

$$\mathbb{K}_{ss} + \mathbb{K}_{sr} \cdot \mathbb{A}_{rs} \cdot (\mathbb{A}_{ss})^{-1} = (\mathbb{A}_{ss})^{-1}, \quad (\text{A22})$$

$$\mathbb{K}_{rs} = -\mathbb{K}_{rr} \cdot \mathbb{A}_{rs} \cdot (\mathbb{A}_{ss})^{-1}. \quad (\text{A23})$$

Then,

$$\mathbb{K}_{ss} + \mathbb{K}_{sr} \cdot \mathbb{A}_{rs} \cdot (\mathbb{A}_{ss})^{-1} = (\mathbb{A}_{ss})^{-1}, \quad (\text{A24})$$

$$-(\mathbb{K}_{rr})^{-1} \cdot \mathbb{K}_{rs} = \mathbb{A}_{rs} \cdot (\mathbb{A}_{ss})^{-1}. \quad (\text{A25})$$

Combining these two equations, we have

$$((\mathbb{K}^{-1})_{ss})^{-1} = (\mathbb{A}_{ss})^{-1} \quad (\text{A26})$$

$$= \mathbb{K}_{ss} - \mathbb{K}_{sr} \cdot (\mathbb{K}_{rr})^{-1} \cdot \mathbb{K}_{rs}. \quad (\text{A27})$$

As a result, $\vec{\alpha}$ is simplified to

$$\vec{\alpha} = ((\mathbb{K}^{-1})_{ss})^{-1} \cdot (P_s^Q)^T \cdot |e_{\text{affine}}\rangle \quad (\text{A28})$$

and the tension response to this external shear is

$$|t\rangle = P_s^Q \cdot ((\mathbb{K}^{-1})_{ss})^{-1} \cdot (P_s^Q)^T \cdot |e_{\text{affine}}\rangle. \quad (\text{A29})$$

Note that this t includes both t^{\parallel} and t^{\perp} , and this formulation applies to other types of homogeneous strain, such as hydrostatic compression, as well.

2. Affine bond deformation in prestressed systems

In this section, we derive the e_{affine} field for any external load represented by a strain tensor ϵ .

We start from the (affine) deformation gradient

$$\Lambda_{ij} \equiv \frac{\partial R_i}{\partial R_{0,j}}, \quad (\text{A30})$$

where the strain tensor $\epsilon = (\Lambda^T \Lambda - I)/2$. The affinely deformed positions of each particle are then

$$\vec{R}_{\ell,\text{affine}} = \Lambda \cdot \vec{R}_{\ell,0}. \quad (\text{A31})$$

We can then use the formulation discussed in Sec. II [Eq.(5)] to calculate the affine extensions/rotations $e_{b,\text{affine}}^{\parallel}$, $e_{b,\text{affine}}^{\perp}$ for each bond, which consist $|e_{\text{affine}}\rangle$.

APPENDIX B: DIPOLE STIFFNESS κ IN PRESTRESSED SYSTEMS

When a pair of dipole forces is applied on a mechanical network between two particles that belong to the same rigid cluster, the network will show a linear response with tension distributed on the bonds. In this Appendix, we derive the stress field of a prestressed network in response to the force dipole,

and obtain a computationally efficient formula that gives the stiffness the system has against this force dipole.

1. Local dipole stiffness

As discussed in Sec. II F, the sum of the external force dipole and the tension response, $|t_{\text{dipole}}\rangle + |t_{\text{rsp}}\rangle$, must be a SSS of the prestressed network,

$$|t_{\text{dipole}}\rangle + |t_{\text{rsp}}\rangle = \sum_i^{N_{\text{SSS}}} \alpha_i |t_{\text{SSS},i}\rangle.$$

The coefficients α_i are determined in the same way as discussed in Appendix A, just by replacing $|e_{\text{aff}}\rangle$ with $|b\rangle$. As a result

$$|t_{\text{dipole}}\rangle + |t_{\text{rsp}}\rangle = P_s^Q \cdot ((\mathbb{K}^{-1})_{ss})^{-1} \cdot (P_s^Q)^T \cdot |b\rangle.$$

We can thus use this in the expression for the dipole stiffness [Eq. (32)], where the denominator is now

$$\begin{aligned} \langle f_{\text{dipole}} | u_{\text{rsp}} \rangle &= -\langle b | \mathbb{K} \mathbb{C} | u_{\text{rsp}} \rangle = -\langle b | t_{\text{rsp}} \rangle \\ &= k_b - \sum_{i,j}^{N_{\text{SSS}}} \langle b | t_{\text{SSS},i} \rangle [(\mathbb{K}^{-1})_{ss}]^{-1} \langle t_{\text{SSS},j} | b \rangle, \end{aligned} \quad (\text{B1})$$

where we used Eq. (29) and the fact that $|t_{\text{rsp}}\rangle = \mathbb{K} \mathbb{C} | u_{\text{rsp}} \rangle$ (bond extension causes tension).

Therefore the dipole stiffness is

$$\begin{aligned} \kappa_b &= \frac{\langle f_{\text{dipole}} | f_{\text{dipole}} \rangle}{\langle f_{\text{dipole}} | u_{\text{rsp}} \rangle} \\ &= \frac{\langle b | \mathbb{K} \mathbb{C} \mathbb{Q} \mathbb{K} | b \rangle}{\langle b | \mathbb{K} | b \rangle - \langle b | \sum_{i,j}^{N_{\text{SSS}}} | t_{\text{SSS},i} \rangle [(\mathbb{K}^{-1})_{ss}]^{-1} \langle t_{\text{SSS},j} | b \rangle} \quad (\text{B2}) \\ &= \frac{2k_b^2}{k_b - \sum_{i,j}^{N_{\text{SSS}}} \langle b | t_{\text{SSS},i} \rangle [(\mathbb{K}^{-1})_{ss}]^{-1} \langle t_{\text{SSS},j} | b \rangle}, \end{aligned}$$

where the factor of 2 in the last line comes from the fact that f_{dipole} involves two particles.

2. Nonlocal dipole stiffness

Besides applying the force dipole on an arbitrary existing bond b in the system, one could also apply a force dipole between two particles which are not connected. As we discuss below, this pair of dipole introduces a new constraint into the system.

Force balance with imposed force dipole $|f_{\text{dipole}}\rangle$ can be written as

$$0 = |f_{\text{dipole}}\rangle + |f_{\text{rsp}}\rangle = |f_{\text{dipole}}\rangle - \mathbb{Q} \mathbb{K} \mathbb{C} | u_{\text{rsp}} \rangle, \quad (\text{B3})$$

where $|u_{\text{rsp}}\rangle$ indicates the particle displacements in response to the force dipole as the system reaches force balance. Unlike the local dipole case discussed above, here f_{dipole} can not be written as $\mathbb{Q} | t_{\text{dipole}} \rangle$ on an existing bond, as the two sites are not connected. Instead, we can introduce an auxiliary bond between the two sites that carry $|f_{\text{dipole}}\rangle$. In this sense, a new constraint and thus a new SSS is added to the system by the auxiliary bond.

Here we introduce the new \mathbb{Q} , \mathbb{C} matrices after introducing the auxiliary bond (which has zero spring constant so that it will not induce tension responses) as

$$\begin{aligned} \tilde{\mathbb{C}} &= \begin{pmatrix} \mathbb{C} \\ C_a \end{pmatrix}, & \tilde{\mathbb{Q}} &= (\mathbb{Q} \quad Q_a), & \tilde{\mathbb{K}} &= \begin{pmatrix} \mathbb{K} & \\ & 0 \end{pmatrix}, \\ \tilde{\mathbb{C}} \cdot |u\rangle &= \begin{pmatrix} |e\rangle \\ e_a \end{pmatrix}, & \tilde{\mathbb{Q}} \cdot \begin{pmatrix} |t\rangle \\ t_a \end{pmatrix} &= -|f\rangle. \end{aligned}$$

The dimension of the bond space is extended with one additional component from the auxiliary bond indexed as a .

Now the force-balanced total tension can be written as

$$|\tilde{t}\rangle = \begin{pmatrix} |t_{\text{rsp}}\rangle \\ t_{\text{dipole}} \end{pmatrix} = \begin{pmatrix} \mathbb{K} \mathbb{C} | u_{\text{rsp}} \rangle \\ t_{\text{dipole}} \end{pmatrix} = \tilde{\mathbb{K}} \tilde{\mathbb{C}} | u_{\text{rsp}} \rangle + |\tilde{t}_{\text{dipole}}\rangle, \quad (\text{B4})$$

where t_{dipole} lives on the auxiliary bond. This $|\tilde{t}\rangle$ satisfies force balance and must be a SSS of the network with the auxiliary bond.

Similar to Appendix A, one can define $P_s^{\tilde{Q}}$, $P_r^{\tilde{Q}}$, $P_s^{\tilde{C}}$, $P_r^{\tilde{C}}$ to the new matrices. We can then decompose the total tension onto SSSs,

$$|\tilde{t}\rangle = \sum_i^{N_{\text{SSS}}} \alpha_i |t_{\text{SSS},i}\rangle = P_s^{\tilde{Q}} \cdot \tilde{\alpha},$$

where $\tilde{\alpha}$'s are coefficients of the linear combination of the SSSs.

We can compute the tension in a similar way,

$$\begin{aligned} (P_s^{\tilde{Q}})^T |\tilde{t}\rangle &= \tilde{\alpha}, \\ (P_r^{\tilde{Q}})^T |\tilde{t}\rangle &= \tilde{0}. \end{aligned}$$

Thus

$$\tilde{0} = (P_r^{\tilde{Q}})^T (\tilde{\mathbb{K}} \tilde{\mathbb{C}} | u_{\text{rsp}} \rangle + |\tilde{t}_{\text{dipole}}\rangle) \quad (\text{B5})$$

$$= (P_r^{\tilde{Q}})^T \tilde{\mathbb{K}} (P_r^{\tilde{Q}} (P_r^{\tilde{Q}})^T + P_s^{\tilde{Q}} (P_s^{\tilde{Q}})^T) \tilde{\mathbb{Q}}^T | u_{\text{rsp}} \rangle + (P_r^{\tilde{Q}})^T |\tilde{t}_{\text{dipole}}\rangle \quad (\text{B6})$$

$$= (P_r^{\tilde{Q}})^T \tilde{\mathbb{K}} P_r^{\tilde{Q}} (P_r^{\tilde{Q}})^T \tilde{\mathbb{Q}}^T | u_{\text{rsp}} \rangle + (P_r^{\tilde{Q}})^T |\tilde{t}_{\text{dipole}}\rangle \quad (\text{B7})$$

$$= \tilde{\mathbb{K}}_{rr} (P_r^{\tilde{Q}})^T \tilde{\mathbb{Q}}^T | u_{\text{rsp}} \rangle + (P_r^{\tilde{Q}})^T |\tilde{t}_{\text{dipole}}\rangle. \quad (\text{B8})$$

As a result,

$$(P_r^{\tilde{Q}})^T \tilde{\mathbb{Q}}^T | u_{\text{rsp}} \rangle = -(\tilde{\mathbb{K}}_{rr})^{-1} (P_r^{\tilde{Q}})^T |\tilde{t}_{\text{dipole}}\rangle. \quad (\text{B9})$$

Note that although the spring constant of the auxiliary bond is 0, the matrix $\tilde{\mathbb{K}}_{rr}$ is still invertible. This is because the auxiliary bond is a redundant bond (otherwise the network would yield, resulting in no stress in linear response), which increases the dimension of the SSSs space and does not introduce new vectors in the orthogonal complement space. As a result, $\tilde{\mathbb{K}}_{rr} = \mathbb{K}_{rr}$ and is invertible.

This can be used to find the coefficients for the SSSs

$$\begin{aligned} \tilde{\alpha} &= (P_s^{\tilde{Q}})^T |\tilde{t}\rangle \\ &= (P_s^{\tilde{Q}})^T (\tilde{\mathbb{K}} \tilde{\mathbb{C}} | u_{\text{rsp}} \rangle + |\tilde{t}_{\text{dipole}}\rangle) \\ &= \tilde{\mathbb{K}}_{sr} (P_r^{\tilde{Q}})^T \tilde{\mathbb{Q}}^T | u_{\text{rsp}} \rangle + (P_s^{\tilde{Q}})^T |\tilde{t}_{\text{dipole}}\rangle \\ &= ((P_s^{\tilde{Q}})^T - \tilde{\mathbb{K}}_{sr} (\tilde{\mathbb{K}}_{rr})^{-1} (P_r^{\tilde{Q}})^T) |\tilde{t}_{\text{dipole}}\rangle, \end{aligned} \quad (\text{B10})$$

where in the last line we used Eq. (B9). These coefficients gives the tension field in response to a nonlocal dipole.

We can then proceed to calculate the dipole stiffness. Applying $P_r^{\tilde{Q}}$ on both sides of Eq. (B9), we have the left-hand side,

$$P_r^{\tilde{Q}}(P_r^{\tilde{Q}})^T \tilde{Q}^T |u\rangle = (\mathbb{I} - P_s^{\tilde{Q}}(P_s^{\tilde{Q}})^T) \tilde{Q}^T |u\rangle \quad (B11)$$

$$= \tilde{Q}^T |u\rangle - P_s^{\tilde{Q}}(\tilde{Q} \cdot P_s^{\tilde{Q}})^T |u\rangle \quad (B12)$$

$$= \tilde{Q}^T |u\rangle. \quad (B13)$$

Equating it to the right-hand side, we have

$$\tilde{Q}^T |u\rangle = -P_r^{\tilde{Q}}(\tilde{\mathbb{K}}_{rr})^{-1} (P_r^{\tilde{Q}})^T |\tilde{t}_{\text{dipole}}\rangle, \quad (B14)$$

expressing the displacement field as a function of the imposed dipole.

One can then compute the nonlocal dipole stiffness κ_a as (the force dipole $|f_{\text{dipole}}\rangle = -\tilde{Q}|\tilde{t}_{\text{dipole}}\rangle \equiv -\tilde{Q}|a\rangle$, where $|a\rangle$ is the vector in the labeling space of bonds which has zeros in all bonds and unity on the a -th component (the auxiliary bond), and a spring constant of unity is added (which is only used

to represent the external force dipole, where the actual spring constant of the auxillary bond regarding its contribution to the network response is still 0 as discussed above),

$$\kappa_a = \frac{\langle f_{\text{dipole}} | f_{\text{dipole}} \rangle}{\langle f_{\text{dipole}} | u \rangle} \quad (B15)$$

$$= \frac{\langle \tilde{t}_{\text{dipole}} | \tilde{Q}^T \tilde{Q} | \tilde{t}_{\text{dipole}} \rangle}{-\langle \tilde{t}_{\text{dipole}} | \tilde{Q}^T | u \rangle} \quad (B16)$$

$$= \frac{\langle \tilde{t}_{\text{dipole}} | \tilde{Q}^T \tilde{Q} | \tilde{t}_{\text{dipole}} \rangle}{\langle \tilde{t}_{\text{dipole}} | P_r^{\tilde{Q}}(\tilde{\mathbb{K}}_{rr})^{-1} (P_r^{\tilde{Q}})^T | \tilde{t}_{\text{dipole}} \rangle} \quad (B17)$$

$$= \frac{\langle a | \tilde{Q}^T \tilde{Q} | a \rangle}{\langle a | P_r^{\tilde{Q}}(\tilde{\mathbb{K}}_{rr})^{-1} (P_r^{\tilde{Q}})^T | a \rangle} \quad (B18)$$

$$= \frac{2}{\langle a | P_r^{\tilde{Q}}(\tilde{\mathbb{K}}_{rr})^{-1} (P_r^{\tilde{Q}})^T | a \rangle}. \quad (B19)$$

The local force dipole response is a special case of nonlocal force dipole response. When considering local force dipoles, the auxiliary bond a overlaps with bond b . One can show that in this case, the nonlocal force dipole stiffness reduces to local force dipole stiffness.

3. Minimum local dipole stiffness $\kappa_{b,\text{min}}$ in prestressed systems

In this section, we derive the minimum dipole stiffness on any given bond b , which is the lowest with respect to the combination of \parallel and \perp directions. To do this, we use (θ, ϕ) to denote the direction of the dipole forces, and the resulting t_{dipole} can be written as

$$|t_{\text{dipole}}\rangle = \begin{pmatrix} 0 \\ \vdots \\ \cos \theta \\ \sin \theta \cos \phi \\ \sin \theta \sin \phi \\ \vdots \\ 0 \end{pmatrix} \equiv |b\rangle, \quad (B20)$$

where we defined the new $|b\rangle$ vector for this case allowing arbitrary force directions. We can plug this $|b\rangle$ in Eq. (B2) to find the dipole stiffness for any given (θ, ϕ) and represent the nontrivial term in κ_b as

$$\eta_b = \langle b | \cdot \sum_{i,j}^{N_{\text{SS}}} |t_{\text{SS},i}\rangle [(\mathbb{K}^{-1})_{\text{ss}}]^{-1} \langle t_{\text{SS},j} | \cdot |b\rangle \equiv \langle b | \mathbb{P} | b \rangle \quad (B21)$$

$$= (0 \quad \dots \quad \cos \theta \quad \sin \theta \cos \phi \quad \sin \theta \sin \phi \quad \dots \quad 0) \cdot \mathbb{P} \cdot \begin{pmatrix} 0 \\ \vdots \\ \cos \theta \\ \sin \theta \cos \phi \\ \sin \theta \sin \phi \\ \vdots \\ 0 \end{pmatrix} \quad (B22)$$

$$= (\cos \theta \quad \sin \theta \cos \phi \quad \sin \theta \sin \phi) \cdot \mathbb{P}_b \cdot \begin{pmatrix} \cos \theta \\ \sin \theta \cos \phi \\ \sin \theta \sin \phi \end{pmatrix}, \quad (B23)$$

where \mathbb{P} represents the matrix in between $|b\rangle$ vectors in Eq. (B21) and \mathbb{P}_b is the 3×3 part of \mathbb{P} associated with bond b .

Similarly,

$$\langle b|\mathbb{K}\mathbb{C}\mathbb{Q}\mathbb{K}|b\rangle = (\cos\theta \quad \sin\theta\cos\phi \quad \sin\theta\sin\phi) \cdot [\mathbb{K}\mathbb{C}\mathbb{Q}\mathbb{K}]_b \cdot \begin{pmatrix} \cos\theta \\ \sin\theta\cos\phi \\ \sin\theta\sin\phi \end{pmatrix},$$

$$\langle b|\mathbb{K}|b\rangle = (\cos\theta \quad \sin\theta\cos\phi \quad \sin\theta\sin\phi) \cdot [\mathbb{K}]_b \cdot \begin{pmatrix} \cos\theta \\ \sin\theta\cos\phi \\ \sin\theta\sin\phi \end{pmatrix},$$

where $[\mathbb{K}\mathbb{C}\mathbb{Q}\mathbb{K}]_b$ and $[\mathbb{K}]_b$ are the 3×3 parts of $\mathbb{K}\mathbb{C}\mathbb{Q}\mathbb{K}$ and \mathbb{K} associated with bond b , respectively.

As a result,

$$\kappa_b = \frac{\langle b|\mathbb{K}\mathbb{C}\mathbb{Q}\mathbb{K}|b\rangle}{\langle b|\sum_{i,j}^{N_{\text{SSS}}} |t_{\text{SSS},i}\rangle [(\mathbb{K}^{-1})_{\text{SS}}]^{-1} \langle t_{\text{SSS},j}|b\rangle}$$

$$= \frac{(\cos\theta \quad \sin\theta\cos\phi \quad \sin\theta\sin\phi) \cdot [\mathbb{K}\mathbb{C}\mathbb{Q}\mathbb{K}]_b \cdot \begin{pmatrix} \cos\theta \\ \sin\theta\cos\phi \\ \sin\theta\sin\phi \end{pmatrix}}{(\cos\theta \quad \sin\theta\cos\phi \quad \sin\theta\sin\phi) \cdot \{[\mathbb{K}]_b - \mathbb{P}_b\} \cdot \begin{pmatrix} \cos\theta \\ \sin\theta\cos\phi \\ \sin\theta\sin\phi \end{pmatrix}}.$$

Minimizing κ_b for a single bond b ,

$$\kappa_{b,\min} = \min_{\theta,\phi} \left[\frac{(\cos\theta \quad \sin\theta\cos\phi \quad \sin\theta\sin\phi) \cdot [\mathbb{K}\mathbb{C}\mathbb{Q}\mathbb{K}]_b \cdot \begin{pmatrix} \cos\theta \\ \sin\theta\cos\phi \\ \sin\theta\sin\phi \end{pmatrix}}{(\cos\theta \quad \sin\theta\cos\phi \quad \sin\theta\sin\phi) \cdot \{[\mathbb{K}]_b - \mathbb{P}_b\} \cdot \begin{pmatrix} \cos\theta \\ \sin\theta\cos\phi \\ \sin\theta\sin\phi \end{pmatrix}} \right] \quad (\text{B24})$$

is an optimization problem with respect to the two variables θ and ϕ . To solve for such optimization problems in our system, we used the Nelder-Mead simplex algorithm as described in Ref. [103]. By doing this minimization, we obtain (θ, ϕ) as the softest dipole stiffness direction for any bond b , which is typically transverse.

-
- [1] S. Alexander, Amorphous solids: their structure, lattice dynamics and elasticity, *Phys. Rep.* **296**, 65 (1998).
- [2] F.-J. Ulm and O. Coussy, Mechanics and durability of solids *Solid Mechanics, Mechanics and Durability of Solids. Solid Mechanics*, Vol. 1 (Prentice Hall, Upper Saddle River, NJ, 2003).
- [3] M. Wyart, L. E. Silbert, S. R. Nagel, and T. A. Witten, Effects of compression on the vibrational modes of marginally jammed solids, *Phys. Rev. E* **72**, 051306 (2005).
- [4] M. Bouzid, J. Colombo, L. V. Barbosa, and E. Del Gado, Elastically driven intermittent microscopic dynamics in soft solids, *Nat. Commun.* **8**, 15846 (2017).
- [5] D. Bi, J. Zhang, B. Chakraborty, and R. P. Behringer, Jamming by shear, *Nature (London)* **480**, 355 (2011).
- [6] P. Sehgal, M. Ramaswamy, I. Cohen, and B. J. Kirby, Using Acoustic Perturbations to Dynamically Tune Shear Thickening in Colloidal Suspensions, *Phys. Rev. Lett.* **123**, 128001 (2019).
- [7] M. Ballauff, J. M. Brader, S. U. Egelhaaf, M. Fuchs, J. Horbach, N. Koumakis, M. Krüger, M. Laurati, K. J. Mutch, G. Petekidis, M. Siebenbürger, T. Voigtman, and J. Zausch, Residual Stresses in Glasses, *Phys. Rev. Lett.* **110**, 215701 (2013).
- [8] M. Gei, A. B. Movchan, and D. Bigoni, Band-gap shift and defect-induced annihilation in prestressed elastic structures, *J. Appl. Phys.* **105**, 063507 (2009).
- [9] Z. Chen, Q. Guo, C. Majidi, W. Chen, D. J. Srolovitz, and M. P. Haataja, Nonlinear Geometric Effects in Mechanical Bistable Morphing Structures, *Phys. Rev. Lett.* **109**, 114302 (2012).
- [10] F. Fraternali, G. Carpentieri, A. Amendola, R. E. Skelton, and V. F. Nesterenko, Multiscale tunability of solitary wave dynamics in tensegrity metamaterials, *Appl. Phys. Lett.* **105**, 201903 (2014).
- [11] A. S. Meeussen, E. C. Oğuz, M. van Hecke, and Y. Shokef, Response evolution of mechanical metamaterials under architectural transformations, *New J. Phys.* **22**, 023030 (2020).
- [12] C. Merrigan, C. Nisoli, and Y. Shokef, Topologically protected steady cycles in an icelike mechanical metamaterial, *Phys. Rev. Res.* **3**, 023174 (2021).
- [13] Z. Wang, K. Li, Q. He, and S. Cai, A light-powered ultralight tensegrity robot with high deformability and load capacity, *Adv. Mater.* **31**, 1806849 (2019).

- [14] S. Armon, E. Efrati, R. Kupferman, and E. Sharon, Geometry and mechanics in the opening of chiral seed pods, *Science* **333**, 1726 (2011).
- [15] M. A. Wyczalkowski, Z. Chen, B. A. Filas, V. D. Varner, and L. A. Taber, Computational models for mechanics of morphogenesis, *Birth Defects Research Part C: Embryo Today: Reviews* **96**, 132 (2012).
- [16] D. Feng, J. Notbohm, A. Benjamin, S. He, M. Wang, L.-H. Ang, M. Bantawa, M. Bouzid, E. Del Gado, R. Krishnan, and M. R. Pollak, Disease-causing mutation in α -actinin-4 promotes podocyte detachment through maladaptation to periodic stretch, *Proc. Natl. Acad. Sci. USA* **115**, 1517 (2018).
- [17] L. Zhang, D. Z. Rocklin, L. M. Sander, and X. Mao, Fiber networks below the isostatic point: Fracture without stress concentration, *Phys. Rev. Mater.* **1**, 052602(R) (2017).
- [18] M. Ozawa, L. Berthier, G. Biroli, A. Rosso, and G. Tarjus, Random critical point separates brittle and ductile yielding transitions in amorphous materials, *Proc. Natl. Acad. Sci. USA* **115**, 6656 (2018).
- [19] V. V. Vasisht, G. Roberts, and E. Del Gado, Emergence and persistence of flow inhomogeneities in the yielding and fluidization of dense soft solids, *Phys. Rev. E* **102**, 010604(R) (2020).
- [20] H. J. Barlow, J. O. Cochran, and S. M. Fielding, Ductile and Brittle Yielding in Thermal and Athermal Amorphous Materials, *Phys. Rev. Lett.* **125**, 168003 (2020).
- [21] E. Berthier, J. E. Kollmer, S. E. Henkes, K. Liu, J. M. Schwarz, and K. E. Daniels, Rigidity percolation control of the brittle-ductile transition in disordered networks, *Phys. Rev. Mater.* **3**, 075602 (2019).
- [22] P. G. Debenedetti and F. H. Stillinger, Supercooled liquids and the glass transition, *Nature (London)* **410**, 259 (2001).
- [23] M. L. Manning and A. J. Liu, Vibrational Modes Identify Soft Spots in a Sheared Disordered Packing, *Phys. Rev. Lett.* **107**, 108302 (2011).
- [24] A. Ninarello, L. Berthier, and D. Coslovich, Models and Algorithms for the Next Generation of Glass Transition Studies, *Phys. Rev. X* **7**, 021039 (2017).
- [25] V. V. Vasisht, P. Chaudhuri, and K. Martens, Residual stress in athermal soft disordered solids: Insights from microscopic and mesoscale models, *arXiv:2108.12782* [cond-mat.soft].
- [26] H. Bhaumik, G. Foffi, and S. Sastry, The role of annealing in determining the yielding behavior of glasses under cyclic shear deformation, *Proc. Natl. Acad. Sci. USA* **118**, e2100227118 (2021).
- [27] D. Richard, M. Ozawa, S. Patinet, E. Stanifer, B. Shang, S. A. Ridout, B. Xu, G. Zhang, P. K. Morse, J.-L. Barrat, L. Berthier, M. L. Falk, P. Guan, A. J. Liu, K. Martens, S. Sastry, D. Vandembroucq, E. Lerner, and M. L. Manning, Predicting plasticity in disordered solids from structural indicators, *Phys. Rev. Mater.* **4**, 113609 (2020).
- [28] E. DeGiuli, A. Laversanne-Finot, G. Düring, E. Lerner, and M. Wyart, Effects of coordination and pressure on sound attenuation, boson peak and elasticity in amorphous solids, *Soft Matter* **10**, 5628 (2014).
- [29] W. G. Ellenbroek, M. van Hecke, and W. van Saarloos, Jammed frictionless disks: Connecting local and global response, *Phys. Rev. E* **80**, 061307 (2009).
- [30] A. J. Licup, S. Münster, A. Sharma, M. Sheinman, L. M. Jawerth, B. Fabry, D. A. Weitz, and F. C. MacKintosh, Stress controls the mechanics of collagen networks, *Proc. Natl. Acad. Sci. USA* **112**, 9573 (2015).
- [31] J. Feng, H. Levine, X. Mao, and L. M. Sander, Alignment and nonlinear elasticity in biopolymer gels, *Phys. Rev. E* **91**, 042710 (2015).
- [32] J. Feng, H. Levine, X. Mao, and L. M. Sander, Nonlinear elasticity of disordered fiber networks, *Soft Matter* **12**, 1419 (2016).
- [33] N. Noll, M. Mani, I. Heemskerk, S. J. Streichan, and B. I. Shraiman, Active tension network model suggests an exotic mechanical state realized in epithelial tissues, *Nat. Phys.* **13**, 1221 (2017).
- [34] C. Hardin, J. Chatteraj, G. Manomohan, J. Colombo, T. Nguyen, D. Tambe, J. J. Fredberg, J. P. Birukov, K. Butler, E. Del Gado, and R. Krishnan, Long-range stress transmission guides endothelial gap formation, *Biochem. Biophys. Res. Commun.* **495**, 749 (2018).
- [35] L. Yan and D. Bi, Multicellular Rosettes Drive Fluid-solid Transition in Epithelial Tissues, *Phys. Rev. X* **9**, 011029 (2019).
- [36] M. Merkel, K. Baumgarten, B. P. Tighe, and M. L. Manning, A minimal-length approach unifies rigidity in underconstrained materials, *Proc. Natl. Acad. Sci.* **116**, 6560 (2019).
- [37] H. Liu, D. Zhou, L. Zhang, D. K. Lubensky, and X. Mao, Topological floppy modes in epithelial tissues, *arXiv:2104.14743*.
- [38] J. Alvarado, M. Sheinman, A. Sharma, F. C. MacKintosh, and G. H. Koenderink, Molecular motors robustly drive active gels to a critically connected state, *Nat. Phys.* **9**, 591 (2013).
- [39] P. Ronceray, C. P. Broedersz, and M. Lenz, Fiber networks amplify active stress, *Proc. Natl. Acad. Sci. USA* **113**, 2827 (2016).
- [40] J.-P. Bouchaud, Granular media: some ideas from statistical physics, *arXiv:cond-mat/0211196*.
- [41] H. Aben, J. Anton, M. Ôis, K. Viswanathan, S. Chandrasekar, and M. M. Chaudhri, On the extraordinary strength of prince rupert's drops, *Appl. Phys. Lett.* **109**, 231903 (2016).
- [42] L. Wen, F. Pan, and X. Ding, Tensegrity metamaterials for soft robotics, *Sci. Robotics* **5**, eabd9158 (2020).
- [43] A. Tanguy, J. P. Wittmer, F. Leonforte, and J.-L. Barrat, Continuum limit of amorphous elastic bodies: A finite-size study of low-frequency harmonic vibrations, *Phys. Rev. B* **66**, 174205 (2002).
- [44] C. S. O'Hern, L. E. Silbert, A. J. Liu, and S. R. Nagel, Jamming at zero temperature and zero applied stress: The epitome of disorder, *Phys. Rev. E* **68**, 011306 (2003).
- [45] M. Wyart, H. Liang, A. Kabla, and L. Mahadevan, Elasticity of Floppy and Stiff Random Networks, *Phys. Rev. Lett.* **101**, 215501 (2008).
- [46] A. J. Liu and S. R. Nagel, The jamming transition and the marginally jammed solid, *Annu. Rev. Condens. Matter Phys.* **1**, 347 (2010).
- [47] K. Chen, M. L. Manning, P. J. Yunker, W. G. Ellenbroek, Z. Zhang, A. J. Liu, and A. G. Yodh, Measurement of Correlations between Low-Frequency Vibrational Modes and Particle Rearrangements in Quasi-Two-Dimensional Colloidal Glasses, *Phys. Rev. Lett.* **107**, 108301 (2011).
- [48] E. Lerner, G. Düring, and M. Wyart, A unified framework for non-Brownian suspension flows and soft amorphous solids, *Proc. Natl. Acad. Sci. USA* **109**, 4798 (2012).

- [49] M. Mosayebi, P. Ilg, A. Widmer-Cooper, and E. Del Gado, Soft Modes and Nonaffine Rearrangements in the Inherent Structures of Supercooled Liquids, *Phys. Rev. Lett.* **112**, 105503 (2014).
- [50] E. Stanifer, P. K. Morse, A. A. Middleton, and M. L. Manning, Simple random matrix model for the vibrational spectrum of structural glasses, *Phys. Rev. E* **98**, 042908 (2018).
- [51] M. Singh, M. Ozawa, and L. Berthier, Brittle yielding of amorphous solids at finite shear rates, *Phys. Rev. Mater.* **4**, 025603 (2020).
- [52] B. P. Tighe, J. H. Snoeijer, T. J. Vlugt, and M. van Hecke, The force network ensemble for granular packings, *Soft Matter* **6**, 2908 (2010).
- [53] R. P. Behringer and B. Chakraborty, The physics of jamming for granular materials: a review, *Rep. Prog. Phys.* **82**, 012601 (2019).
- [54] J. H. Snoeijer, T. J. H. Vlugt, M. van Hecke, and W. van Saarloos, Force Network Ensemble: A New Approach to Static Granular Matter, *Phys. Rev. Lett.* **92**, 054302 (2004).
- [55] B. P. Tighe, A. R. T. van Eerd, and T. J. H. Vlugt, Entropy Maximization in the Force Network Ensemble for Granular Solids, *Phys. Rev. Lett.* **100**, 238001 (2008).
- [56] D. Bi, S. Henkes, K. E. Daniels, and B. Chakraborty, The statistical physics of athermal materials, *Annu. Rev. Condens. Matter Phys.* **6**, 63 (2015).
- [57] S. F. Edwards and R. Oakeshott, Theory of powders, *Physica A* **157**, 1080 (1989).
- [58] X. Mao, P. M. Goldbart, X. Xing, and A. Zippelius, Elastic heterogeneity of soft random solids, *Europhys. Lett.* **80**, 26004 (2007).
- [59] S. Henkes and B. Chakraborty, Statistical mechanics framework for static granular matter, *Phys. Rev. E* **79**, 061301 (2009).
- [60] X. Mao, P. M. Goldbart, X. Xing, and A. Zippelius, Soft random solids and their heterogeneous elasticity, *Phys. Rev. E* **80**, 031140 (2009).
- [61] A. Lemaître, Inherent stress correlations in a quiescent two-dimensional liquid: Static analysis including finite-size effects, *Phys. Rev. E* **96**, 052101 (2017).
- [62] M. Maier, A. Zippelius, and M. Fuchs, Emergence of Long-Ranged Stress Correlations at the Liquid to Glass Transition, *Phys. Rev. Lett.* **119**, 265701 (2017).
- [63] E. DeGiuli, Field Theory for Amorphous Solids, *Phys. Rev. Lett.* **121**, 118001 (2018).
- [64] J. N. Nampoothiri, Y. Wang, K. Ramola, J. Zhang, S. Bhattacharjee, and B. Chakraborty, Emergent Elasticity in Amorphous Solids, *Phys. Rev. Lett.* **125**, 118002 (2020).
- [65] B. A. DiDonna and T. C. Lubensky, Nonaffine correlations in random elastic media, *Phys. Rev. E* **72**, 066619 (2005).
- [66] S. Pellegrino and C. R. Calladine, Matrix analysis of statically and kinematically indeterminate frameworks, *Int. J. Solids Struct.* **22**, 409 (1986).
- [67] K. Sun, A. Souslov, X. Mao, and T. Lubensky, Surface phonons, elastic response, and conformal invariance in twisted kagome lattices, *Proc. Natl. Acad. Sci. USA* **109**, 12369 (2012).
- [68] T. Lubensky, C. Kane, X. Mao, A. Souslov, and K. Sun, Phonons and elasticity in critically coordinated lattices, *Rep. Prog. Phys.* **78**, 073901 (2015).
- [69] D. M. Sussman, C. P. Goodrich, and A. J. Liu, Spatial structure of states of self stress in jammed systems, *Soft Matter* **12**, 3982 (2016).
- [70] C. R. Calladine, Buckminster fuller's "tensegrity" structures and clerk maxwell's rules for the construction of stiff frames, *Int. J. Solids Struct.* **14**, 161 (1978).
- [71] C. Kane and T. Lubensky, Topological boundary modes in isostatic lattices, *Nat. Phys.* **10**, 39 (2014).
- [72] D. Z. Rocklin, S. Zhou, K. Sun, and X. Mao, Transformable topological mechanical metamaterials, *Nat. Commun.* **8**, 14201 (2017).
- [73] L. Zhang and X. Mao, Fracturing of topological maxwell lattices, *New J. Phys.* **20**, 063034 (2018).
- [74] D. Zhou, L. Zhang, and X. Mao, Topological Edge Floppy Modes in Disordered Fiber Networks, *Phys. Rev. Lett.* **120**, 068003 (2018).
- [75] J. Ma, D. Zhou, K. Sun, X. Mao, and S. Gonella, Edge Modes and Asymmetric Wave Transport in Topological Lattices: Experimental Characterization at Finite Frequencies, *Phys. Rev. Lett.* **121**, 094301 (2018).
- [76] X. Mao and T. C. Lubensky, Maxwell lattices and topological mechanics, *Annu. Rev. Condens. Matter Phys.* **9**, 413 (2018).
- [77] D. Zhou, L. Zhang, and X. Mao, Topological Boundary Floppy Modes in Quasicrystals, *Phys. Rev. X* **9**, 021054 (2019).
- [78] D. Zhou, J. Ma, K. Sun, S. Gonella, and X. Mao, Switchable phonon diodes using nonlinear topological maxwell lattices, *Phys. Rev. B* **101**, 104106 (2020).
- [79] K. Sun and X. Mao, Continuum Theory for Topological Edge Soft Modes, *Phys. Rev. Lett.* **124**, 207601 (2020).
- [80] R. Connelly and W. Whiteley, The stability of tensegrity frameworks, *Int. J. Space Struct.* **7**, 153 (1992).
- [81] E. Lerner, Quasilocalized states of self stress in packing-derived networks, *Eur. Phys. J. E* **41**, 93 (2018).
- [82] C. Rainone, E. Bouchbinder, and E. Lerner, Statistical mechanics of local force dipole responses in computer glasses, *J. Chem. Phys.* **152**, 194503 (2020).
- [83] E. DeGiuli and J. McElwaine, Laws of granular solids: Geometry and topology, *Phys. Rev. E* **84**, 041310 (2011).
- [84] B. Cui, G. Ruocco, and A. Zaccone, Theory of elastic constants of athermal amorphous solids with internal stresses, *Granular Matter* **21**, 1 (2019).
- [85] G. Bordiga, L. Cabras, A. Piccolroaz, and D. Bigoni, Dynamics of prestressed elastic lattices: Homogenization, instabilities, and strain localization, *J. Mech. Phys. Solids* **146**, 104198 (2021).
- [86] J. D. Weeks, D. Chandler, and H. C. Andersen, Role of repulsive forces in determining the equilibrium structure of simple liquids, *J. Chem. Phys.* **54**, 5237 (1971).
- [87] V. V. Vasisht and E. Del Gado, Computational study of transient shear banding in soft jammed solids, *Phys. Rev. E* **102**, 012603 (2020).
- [88] S. Plimpton, Fast parallel algorithms for short-range molecular dynamics, *J. Comput. Phys.* **117**, 1 (1995).
- [89] L. V. Foster and T. A. Davis, Algorithm 933: Reliable calculation of numerical rank, null space bases, pseudoinverse solutions, and basic solutions using suitesparseqr, *ACM Trans. Math. Softw.* **40**, 1 (2013).
- [90] <https://people.engr.tamu.edu/davis/suitesparse.html>.

- [91] B. Hopkins and J. G. Skellam, A new method for determining the type of distribution of plant individuals, *Ann. Botany* **18**, 213 (1954).
- [92] F. Leonforte, A. Tanguy, J. P. Wittmer, and J.-L. Barrat, Continuum limit of amorphous elastic bodies ii: Linear response to a point source force, *Phys. Rev. B* **70**, 014203 (2004).
- [93] C. E. Maloney and A. Lemaître, Amorphous systems in athermal, quasistatic shear, *Phys. Rev. E* **74**, 016118 (2006).
- [94] S. S. Schoenholz, A. J. Liu, R. A. Riggelman, and J. Rottler, Understanding Plastic Deformation in Thermal Glasses from Single-Soft-Spot Dynamics, *Phys. Rev. X* **4**, 031014 (2014).
- [95] C. Rainone, E. Bouchbinder, and E. Lerner, Pinching a glass reveals key properties of its soft spots, *Proc. Natl. Acad. Sci. USA* **117**, 5228 (2020).
- [96] E. D. Cubuk, S. S. Schoenholz, J. M. Rieser, B. D. Malone, J. Rottler, D. J. Durian, E. Kaxiras, and A. J. Liu, Identifying Structural Flow Defects in Disordered Solids Using Machine-Learning Methods, *Phys. Rev. Lett.* **114**, 108001 (2015).
- [97] R. Seto, R. Mari, J. F. Morris, and M. M. Denn, Discontinuous Shear Thickening of Frictional Hard-Sphere Suspensions, *Phys. Rev. Lett.* **111**, 218301 (2013).
- [98] M. Wyart and M. E. Cates, Discontinuous Shear Thickening without Inertia in Dense Non-Brownian Suspensions, *Phys. Rev. Lett.* **112**, 098302 (2014).
- [99] N. Y. Lin, C. Ness, M. E. Cates, J. Sun, and I. Cohen, Tunable shear thickening in suspensions, *Proc. Natl. Acad. Sci. USA* **113**, 10774 (2016).
- [100] B. M. Guy, J. A. Richards, D. J. M. Hodgson, E. Blanco, and W. C. K. Poon, Constraint-Based Approach to Granular Dispersion Rheology, *Phys. Rev. Lett.* **121**, 128001 (2018).
- [101] K. Liu, J. E. Kollmer, K. E. Daniels, J. M. Schwarz, and S. Henkes, Spongelike Rigid Structures in Frictional Granular Packings, *Phys. Rev. Lett.* **126**, 088002 (2021).
- [102] M. Ramaswamy, I. Griniasty, D. B. Liarte, A. Shetty, E. Katifori, E. Del Gado, J. P. Sethna, B. Chakraborty, and I. Cohen, Universal scaling of shear thickening transitions, [arXiv:2107.13338](https://arxiv.org/abs/2107.13338).
- [103] J. C. Lagarias, J. A. Reeds, M. H. Wright, and P. E. Wright, Convergence properties of the nelder–mead simplex method in low dimensions, *SIAM J. Opt.* **9**, 112 (1998).